

Overview of JET Results

F. Romanelli, R. Kamendje^a on behalf of JET-EFDA Contributors¹

JET-EFDA, Culham Science Centre, Abingdon, OX14 3DB, UK

^a Also: Institut für Theoretische Physik-Computational Physics, Technische Universität Graz, Petersgasse 16, A- 8010 Graz, Austria

E-mail of corresponding author: Richard.kamendje@jet.efda.org

Abstract

Since the last IAEA, the scientific programme of JET has focussed on the qualification of the integrated operating scenarios for ITER and on physics issues essential for the consolidation of design choices and the efficient exploitation of ITER. Particular attention has been given to the characterisation of the edge plasma, pedestal energy and Edge Localised Modes (ELMs), and their impact on plasma facing components (PFCs). Various ELM mitigation techniques have been assessed for all ITER operating scenarios using active methods such as resonant magnetic field perturbation, rapid variation of the radial field and pellet pacing. In particular, the amplitude and frequency of Type I ELMs have been actively controlled over a wide parameter range ($q_{95}=3-4.8$, $\beta_N \leq 3.0$) by adjusting the amplitude of the $n=1$ external perturbation field induced by Error Field Correction Coils. The study of disruption induced heat loads on PFCs has taken advantage of a new wide-angle viewing infra-red system and a fast bolometer to provide a detailed account of time, localisation and form of the energy deposition. Specific ITER-relevant studies have used the unique JET capability of varying the Toroidal Field (TF) ripple from its normal low value $\delta_{BT}=0.08\%$ up to $\delta_{BT}=1\%$ to study the effect of TF ripple on high confinement-mode plasmas. The results suggest that $\delta_{BT}<0.5\%$ is required on ITER to maintain adequate confinement to allow $Q_{DT}=10$ at full field. Physics issues of direct relevance to ITER include heat and toroidal momentum transport, with experiments using power modulation to decouple power input and torque to achieve first experimental evidence of inward momentum pinch and determine the threshold for ion temperature gradient driven modes. Within the longer term JET programme in support of ITER, activities aiming at the modification of the JET first wall and divertor and the upgrade of the neutral beam and plasma control systems are being conducted. The procurement of all components will be completed by 2009 with the shutdown for the installation of the beryllium wall and tungsten divertor extending from summer 2009 to summer 2010.

1 Introduction

The JET programme is devoted to the qualification of the integrated operating scenarios for ITER and the consolidation of ITER design choices. Since the last IAEA conference three experimental campaigns have been executed. The reliability of the various systems (heating and fuelling, power supplies, etc...) has been very satisfactory, with record performance delivered in many areas. This has allowed substantial progress to be made in a number of physics topics. Plasma scenarios up to $I_p=3.8\text{MA}$ plasma current have been investigated. Furthermore, specific JET capabilities, such as the possibility of producing variable toroidal field ripple, have been fully exploited.

The first key issue, addressed in Section 2, is the performance of the ITER operating scenarios [1] including the baseline scenario (high confinement mode, H-mode, with MHD instabilities in the core (sawteeth) and in the edge (Edge Localised Modes, ELMs)) and the more advanced scenarios which offer potential for improved performance, long pulse operation and steady state. With regard to the ELMy H-mode scenario, emphasis is given on extending high triangularity plasmas ($\delta \sim 0.45$) to higher currents (up to 3.8MA) in order to characterise the performance, edge, pedestal and ELMs. With regard to the hybrid regime (in ITER, H-mode regime operated at slightly lower plasma current), tailoring the q profile has lead to the achievement of substantially improved confinement relative to the reference baseline H-mode scenario, $H_{98}(y,2) \sim 1.35$ for $\sim 6\text{s}$. Furthermore, investigations on JET have

¹ See Appendix

focussed on extending the edge safety factor q , the density and the normalised pressure (β_N) range of this scenario, and making systematic comparisons of these discharges with a reference baseline H-mode scenario. The main fields of development of the advanced tokamak (AT) scenario (candidate for steady-state operation in ITER) in JET have been the compatibility of this scenario with an ITER-like beryllium wall and tungsten divertor and the role of the q profile shape for accessing high β_N operational domains beyond the experimental “no-wall MHD limit”. The second key issue, addressed in Section 3, is that of achieving acceptable wall power and particle loadings (fuel retention) in conjunction with high fusion performance. ELMs associated with the ITER baseline scenario will cause erosion and damage to plasma facing components (PFCs) and it is essential to develop active mitigation techniques applicable to a as wide as possible range of ITER plasma parameters. JET has applied a number of such techniques to successfully mitigate the impact of Type I ELMs, including the use of resonant magnetic perturbation, the rapid variation of the radial magnetic field using the vertical stabilisation controller and impurity seeding. Heat loads and forces induced on in-vessel components by disruptive events in ITER are also expected to pose a limit to their life time. JET has used new diagnostics such as a new wide-angle viewing infrared system and a fast bolometer to provide a detailed account of time, localisation and form of the energy deposition on PFCs, and halo current sensors to provide better understanding of the dynamics of plasma-wall interaction during a vertical displacement event. The third key issue, addressed in Section 4, is the effect of toroidal field (TF) ripple on H-mode plasmas in view of determining the maximum TF ripple that can be tolerated on ITER. To this end, JET has used its unique capability of varying the TF ripple from its normal low value $\delta_{BT}=0.08\%$ up to $\delta_{BT}=1\%$. The fourth key issue, discussed in Section 5, is the role of plasma rotation and momentum transport on confinement and turbulence, given that plasma rotation is predicted to be low in ITER. Experiments at JET have used power modulation using neutral beam (NB) injection and/or ion cyclotron resonance heating (ICRH) in order to decouple power input and torque and to (i) quantify the momentum diffusivity and pinch; (ii) determine the threshold for ion temperature gradient driven modes; (iii) study temperature profile stiffness with plasma rotation. Furthermore, variation of the TF ripple has been used to investigate the role of rotation in the sustainment and strength of internal transport barriers (ITB). The final key issue in this paper, discussed in Section 6, is the coupling of ion cyclotron resonance frequency (ICRF) and lower hybrid (LH) power into ELMy H-mode plasmas in JET in ITER-relevant conditions, i.e., at large antenna-plasma distances. Section 7 outlines the plan for the JET enhancement programme in support of ITER.

2 Physics developments for ITER scenarios

ITER scenarios development on JET has benefited from the very good performance of the auxiliary heating systems and the increased shaping capability following the modifications leading to the Mark II HD divertor. The number of discharges in this period with injected NB power above 20MW is more than three times the one achieved previously, see figure 1. Moreover, during the campaigns covered in this report, additional time has been devoted to conditioning of the LH system. As a result the performance of this system in terms of power density has been brought back to the ITER-relevant level of 24MW/m² at 3.7 GHz with 5.7MW of power so far coupled to L-mode plasmas, a value which was last achieved in 1996.

2.1 ELMy H-mode

At high triangularity, $\delta \sim 0.45$, the ELMy H-mode regime has been investigated at high plasma current up to 3.5MA/3.2T ($q_{95} \sim 2.9$, Type I ELMs with energy up to $W_{ELM} \sim 0.6$ MJ, plasma stored energy ~ 9.5 MJ). The overall plasma performances appear to be similar to those

obtained with earlier high δ configurations (HT3), suggesting that, in JET, an optimum has been reached in terms of confinement with regard to the plasma shape probably due to a stronger effect of recycling flux in the ITER-like shape, imputable to the reduced distance ($<0.1\text{m}$) between the X-point and the inner vertical divertor target tiles. So far, at low $\delta \sim 0.25$, plasma currents up to $3.8\text{MA}/3.2\text{T}$ ($q_{95} \sim 2.75$, Type I ELM energy $W_{\text{ELM}} \sim 1\text{MJ}$, plasma stored energy $\sim 10\text{MJ}$) have been achieved (figure 2). These plasmas allow access to both low normalised ion Larmor radius ρ^* (~ 0.0035) and collisionality ν^* (~ 0.04). Documenting the pedestal characteristics in this parameter space has been possible thanks to improved diagnostic capabilities such as the high resolution Thomson scattering diagnostic (HRTS) and the upgraded electron cyclotron emission (ECE) radiometer, which have enabled pedestal profiles to be resolved for an extended range of plasma conditions [2]. While figure 3 shows typical profiles obtained at $3.8\text{MA}/3.2\text{T}$ with pedestal electron temperature T_e of 2.5keV and electron density n_e of $5 \times 10^{19}\text{m}^{-3}$, figure 4 gives an overview of the measured range in the parameter space defined by the pedestal average n_e and T_e . The time evolution of the pedestal n_e and T_e as observed during a typical Type I ELM crash is discussed in Section 3.1 as well as the associated conductive and convective losses. The pedestal properties are found to have a crucial impact on global plasma performance, in particular with regard to the β dependence of confinement as shown in Ref. [3] for the hybrid scenario.

2.2 Hybrid scenario

In the first JET experiments on the hybrid scenario in 2003-2004 the parameter space of this scenario has been limited to $q_{95}=4$, relatively short duration ($\sim 4\text{s}$, not exceeding the resistive time), moderate density with respect to the Greenwald density limit ($n_e/n_{\text{GW}} \sim 0.5-0.6$, $n_{\text{GW}}=I_p/(\pi a^2)$) and a total normalised pressure β_N of 2.8 (i.e. typically below the estimated no wall stability limit given by the product $4 \times l_i$ with l_i being the internal inductance). In recent experiments, this parameter space has been substantially extended ($2.7 \leq q_{95} \leq 4.5$, β_N up to 3.6, density up to the Greenwald limit at $\beta_N=2.7$, discharge duration up to 20s at $\beta_N=2.5$) [4]. This extension of the parameter space in a large machine like JET is crucial for the development of the hybrid scenario closer to ITER parameters at lower ρ^* and ν^* . Figure 5 illustrates the extension in JET in terms of β_N and ρ^* with respect to the 2003-2004 data. Prior to the 2008 experimental campaigns, it appeared that in all this parameter space the confinement had not shown any sign of improvement above 1.1 with respect to the $H_{98}(y,2)$ scaling, in contrast to results reported from other devices such as ASDEX Upgrade and DIII-D. This fact had thus triggered in 2007 a systematic comparison of these discharges with a reference H-mode scenario at same toroidal field strength (1.7T) and different plasma current I_p ranging from 1.4MA to 2MA. This comparison has been achieved with a plasma shape at high triangularity of $\delta=0.45$ and up to normalised pressure β_N of 3.0. For both the hybrid scenario and its equivalent H-mode stationary conditions were obtained for about one resistive time with the figure of merit for fusion gain ($H_{89}\beta_N/q_{95}^2$) reaching up to 0.7 at $q_{95}=2.8$. The distinction between the two scenarios has been made operationally by applying current penetration control for the hybrid scenario and fully diffused q profile for the H-mode. As can be seen in figure 6 which shows a superposition of time traces of discharges from the two different scenarios, the comparison pointed out no differences in thermal confinement, though hybrid discharges are less affected by neoclassical tearing modes. However, as shown in figure 7, the q profiles of both scenarios were found almost identical after about one resistive time ($\tau_R \sim 6\text{s}$) indicating that the modifications operated on the q profile in the current ramp-up (weak magnetic shear in the plasma core within $r/a \sim 0.4$) in the hybrid scenario may not be relevant in changing the transport in the plasma core. Therefore, experiments in 2008 set out to investigate possible routes for tailoring the q profile in hybrid discharges such as strong variations of the q profile produced using strong current ramp down (0.6MA/s) after an initial

current ramp up (from 0.3 to 0.5MA/s). This has the effect to reduce the inductive flux in the outer half of the plasma ($r/a > 0.5$) and results in a significant broadening of the q profile and a sharp steepening of the magnetic shear in this region as can be seen in figure 8. Results achieved so far indicate improved confinement of $H_{98}(y,2) > 1.35$ for ~ 6 s (figure 9) at both low and high triangularity with transient peak values of $H_{98}(y,2)$ reaching up to 1.45 for 1s.

With regard to the stability of the hybrid scenario in JET, dedicated experiments with preformed target q profile close to unity and reduced toroidal field strength ($B_T = 1.5$ T) have extended the scenario operations at higher total normalised pressure (up to $\beta_N = 3.6$). In contrast to other devices such as DIII-D or JT-60U, this high normalised pressure has been reached without significant 2/1 NTM activity. This value of β_N is also well above $4\bar{\iota}_i$. The proximity to the no-wall limit has been diagnosed in these plasmas using the Resonant Field Amplification (RFA) of an externally applied helical magnetic field. Figure 10 shows the plasma response of the radial magnetic field to an applied perturbation with the JET Error Field Correction Coils (EFCCs) in AC mode with a probing frequency of 20Hz. At about 28-29s this response increases and looks consistent with β_N exceeding the estimated ideal limit of $4\bar{\iota}_i$.

The integrity of the hybrid scenario has also been investigated in an attempt to demonstrate, on the one hand, that the combination of non-inductive current drive sources can preserve the initial (optimised) q profile for duration exceeding several resistive times and, on the other hand, the compatibility this scenario with power handling limits imposed by metallic materials in the future ITER-like wall in JET (see Section Outlook). In order to make hybrid discharges compatible with long duration, the new JET shape controller recently installed and validated for accurate control of the plasma boundary has been integrated with boundary flux control and also includes a strike point sweeping facility specifically designed to spread the heat load on the divertor target (see ref. [4] and references therein). Figure 11 illustrates a long hybrid discharge in JET with $q \sim 1$, operated at $I_p = 1.3$ MA and $B_T = 1.5$ T with ITER-like magnetic configuration ($\delta \sim 0.4$) and $q_{95} = 3.5$. This discharge 14 reaches a normalised pressure β_N of 2.5 for almost 20s (more than 3 resistive times). During the 20s pulse, both boundary flux control and sweeping have been applied at a rate of 0.15Wb/s. The strike points are swept with peak to peak amplitude of 7cm and a frequency of 4Hz on two tiles of the divertor. Infrared camera measurements show that the maximum temperature on the outer divertor tile is lowered by 25 to 30% close to thermal equilibrium conditions. The broadening of the foot print on the tile results in a lower power load density from typically 5MW/m² to 3.5MW/m². On average, no significant confinement losses related to the sweeping of the strike points are observed. However, to ensure compatibility with an all-metal wall this scenario will require line average density higher than the beam shinethrough limits.

2.3 Advanced tokamak scenarios

Before 2006, AT scenario research on JET concentrated on low triangularity plasmas with deeply reversed q profiles, with “strong” ITB and type III ELMs H-mode. Starting in 2006, the focus has shifted towards the exploration and integration of ITER-relevant issues such as (i) the operation at ITER-relevant $q_{95} \sim 5$ and high triangularity, (ii) the approach to high normalised pressure, the maximisation of the self-generated Bootstrap current and the investigation of MHD stability limits, (iii) the exploration of ITB physics at higher density and (iv) the investigation of weakly reversed q profiles and ITBs located at large minor radius. Access to high β_N plasmas, with or without ITBs, has been investigated at high triangularity, $\delta \sim 0.35$ -0.5, and high density, $n_G \sim 0.5$ -0.8, at $I_p = 1.2$ -1.8MA / $B_T = 1.8$ -2.7T ($q_{95} \sim 5$) [5]. The current profile is tailored via a fast current ramp, ohmic or with Lower Hybrid Current Drive (LHCD), and early application of NBI or NBI+ICRH power. The resulting target q profile at

the start of the main NBI heating phase has low or weakly negative magnetic shear in the core and the minimum value of q (q_{\min}) is adjusted using the start time of the NBI pulse. In these experiments $\beta_N \sim 3$ was sustained for up to $\sim 18\tau_E$ (τ_E is the energy confinement time) and $\beta_N \sim 2.8$ for up to $\sim 35\tau_E$ ($\sim 1\tau_R$) and was limited by the allowed NBI pulse length for this particular configuration, with $H_{98}(y,2) \sim 1.0-1.2$ (see figures 12 and 13). The development of an ITB contributes by 20-25% to β_N , the best performance being obtained when an ITB forms in both ion and electron temperature channels. The total non-inductive current fraction reaches transiently 75% at the maximum values of β_N and $>60\%$ in a more stationary phase. Discharges are routinely obtained with total β_N above the no-wall β -limit, determined theoretically by modelling and empirically by observing resonant field amplification of an externally applied magnetic perturbation [6]. The measured β -limit and the achievable β both decrease with increasing q_{\min} (see for instance figure 14), as do the global confinement and the core pressure. Edge control for AT operation and compatibility with ITER wall material conditions have been investigated using different techniques [7]: (i) Injection of high-Z radiative gas, such as neon, to increase the edge radiation [8]. Two regimes with mild ELM activity have been found at a power radiation fraction either $P_{\text{rad}}/P_{\text{tot}} \sim 30\%$, with high frequency Type I ELMs, or at $P_{\text{rad}}/P_{\text{tot}} \geq 50\%$, with Type III ELMs or an L-mode edge. With its radiation level mainly determined by carbon it is not obvious that the first regime at $P_{\text{rad}}/P_{\text{tot}} \sim 30\%$ could be directly translated to future experiments with the foreseen ITER-like wall (ILW) in JET [9]. Regimes at $P_{\text{rad}}/P_{\text{tot}} \geq 50\%$ usually require higher core confinement to compensate for the reduction of pedestal energy; (ii) Sweeping of the strike points to spread the heat load on the divertor tiles [10]. Since the PFCs are not actively cooled on JET, this scheme will be used for the development of the 20s high power discharges (45MW) foreseen after the completion of the NBI power enhancement [11]; (iii) Change of the magnetic configuration to quasi-double null plasmas able to reach a grassy ELM regime. This regime has been combined with core ITB on the ion heat transport channel but the achievement of $q_{95} \sim 5$ has not been achieved so far due to the lack of additional heating power; (iv) Resonant magnetic perturbation at the plasma edge [12] (see Section 3.2.1), with the reduction in confinement at the edge transport barrier compensated by an increase of the core energy content.

2.4 ITER current ramp studies

The experimental verification of ITER scenarios in JET includes [13] studies of (i) the plasma initiation at low voltage; (ii) the current rise phase; (iii) the performance during the flat top phase of the H-mode reference scenario at $q_{95} \sim 3$ as well as the hybrid scenario at $q_{95} \sim 4$; (iv) the ramp down of the plasma. With regard to (i) JET results show that the minimum electric field on axis for reliable ohmic (un-assisted) breakdown is $E \sim 0.23\text{V/m}$, well below the ITER design value (0.33V/m). Reliable assisted breakdown with 1MW of LHCD (no ionisation of the filling gas is observed) has also been established at electric field values down to $E \sim 0.19\text{V/m}$ (below the ITER value of 0.32V/m) as shown in figure 15. In reducing the available loop voltage, the plasma initiation is delayed by 50ms-100ms and a slow and linear rise of the plasma current is observed. Using low voltage schemes, breakdown is still achievable after a high current ($q_{95}=3$) disruption (previous pulse). By adjusting the prefill at 0.33V/m and using 1MW LHCD assist, plasma initiation is successful, albeit at somewhat higher plasma density with a resulting slower rise of the plasma current compared to clean vessel conditions.

With regard to (ii) figure 16 shows that low plasma inductance is only achieved with a full bore limiter phase (limited on the outboard side to reproduce ITER conditions) and diverting as early as possible. This also allows early use of additional heating during the divertor phase. Moreover, it is found that at fixed plasma shape ohmic discharges reach $q_{95} \sim 3$ with the lowest

internal inductance $l_i=0.83$ when using the fastest current ramp rates available (0.36MA/s). These results extrapolate to ITER having a fast current rise time to 15 MA of ~ 70 s and a slow rise phase of ~ 100 s. As shown in figure 17, in JET experiments, the use of additional heating during the current rise, in L-mode or in H-mode, gives a capability of significantly varying $l_i(3)$, with no difference in the $l_i(3)$ achieved at $q_{95}=3$ using 3MW central ICRH, 2.2MW LHCD or 4 MW NBI. Furthermore, the control of $l_i(3)$ by additional heating has been demonstrated with either ICRH or NBI in scenarios with a current rise to $q_{95}=4$ (2MA/2.4T). As shown in figure 18, requesting $l_i(3)=0.8$, a target q-profile with $q(0)$ just above 1 at the start of the flat top is produced requiring modest heating powers (ICRH ~ 3 MW, NBI ~ 5 MW). During the flat top phase (iii) experiments have reproduced the requirements for reaching $Q_{DT}=10$ at $q_{95}=3$: $H_{98}(y,2)\sim 1$, $\beta_N\sim 1.8$ [13].

With regard to the current decay phase (iv), experiments clearly show that in ohmic and L-mode conditions only a very slow current ramp down can keep $l_i<1.6$ during the first half of the current decay. Extrapolated to ITER, a 300s ramp down phase would be required, likely to consume transformer flux. Preliminary results show that, in scenarios that maintain H-mode throughout the ramp down phase, the current can be ramped down without additional flux consumption while keeping l_i low enough using modest ramp down rates. Therefore, the requirements for the heating systems in ITER to provide sufficient power to stay in H-mode during most of the ramp down phase need to be assessed.

3 First wall power and particle loadings

3.1 ELMs and their impact on plasma facing components

The Type I ELMs associated with the ITER baseline scenario will cause erosion and damage to the PFCs. To ensure sufficient divertor target lifetime, the loss in plasma stored energy due to ELMs in ITER should be restricted to $\Delta W_{ELM}\sim 1$ MJ. To access the highest possible ΔW_{ELM} , JET has been run at $I_p=3.0$ MA ($B_T=3$ T, $q_{95}\sim 3.1$) in a series of dedicated discharges with fixed plasma shape ($\delta=0.25$, elongation $\kappa=1.72$), progressively decreasing the gas fuelling, Γ_{gas} , from shot to shot. This produces a scan in ELM amplitude and frequency at high plasma stored energy W_{plasma} (~ 8 MJ) with the largest $\Delta W_{ELM}\sim 0.8-0.9$ MJ being found at $\Gamma_{gas}=0$, for which the plasma density reaches only ~ 0.4 of the Greenwald limit [14]. As can be seen in figure 19, the largest ELMs are generally sporadic and often compound, characterised by a sharp initial drop in W_{plasma} (see also figure 20a) and followed by a phase of smaller ELMs (possibly Type III), during which stored energy decays on a longer timescale, and resulting in a decrease in the $H_{98}(y,2)$ factor from ~ 1.2 to ~ 1.0 , although no deleterious effects of impurity release is observed. The ELMs provoke strong radiation losses, mostly confined to the inner divertor volume (figure 20b). The amount of energy radiated during/after the ELM, as a fraction of the ELM energy is found to vary from about half for $\Delta W_{ELM}\leq 0.6$ MJ to larger values (approaching 100% for large, compound ELMs), suggesting thermal decomposition of re-deposited layers on the inner divertor target and ablation of target plates. The largest ELMs appear to deposit no more than 10% of the lost energy on the outer wall of the main chamber, an energy fraction which is well reproduced by the model of ELM filament parallel energy losses [15]. Now seen in all tokamaks where they have been sought and on a variety of diagnostics at JET [16, 17, 2] (see also figure 21), ELM filaments convecting plasma rapidly across the magnetic field in the Scrape-Off Layer (SOL) to main chamber surfaces are a concern for ITER [18]. Type I ELM filaments are found to follow pre-ELM magnetic field lines, i.e. they do not noticeably distort/perturb the SOL (poloidal/toroidal) magnetic field, and most likely do not carry all the energy and particles expelled by an ELM collapse [2]. Inspection of infra-red images from the wide-angle viewing system obtained in the discharges discussed here reveals essentially no ELM interaction with the upper dump plates and none on

the inner wall. By far the largest deposition occurs on the divertor targets, but there is a non-negligible interaction with the low field side bumper limiters. A new divertor infra-red camera, installed in JET after the series of discharges discussed above were performed, now allows a detail study of the ELM power load evolution on divertor targets. Figure 22a shows the present divertor target geometry at JET and indicates the areas covered by the IR divertor viewing system which uses a top window. Using a physics-based model describing Type-I ELM energy transport to the divertor and the first wall [19] the ELM power deposition time on the inner/outer divertor targets (τ_{IR}) is found to be entirely determined by pedestal ions free-streaming to the divertor targets. The fraction of energy deposited on the target within the range $0 < t < \tau_{IR}$ varies between 20% for the largest ELMs (lowest pedestal collisionality) and 35% for smallest ELMs (highest pedestal collisionality) [17]. Within this model the observed type-I ELM in/out power load asymmetries in figure 22b can be described as given by an initial parallel Mach number of the particles released in the scrape off layer (SOL) during an ELM, which is attributed to the pre-ELM pedestal plasma rotation [17]. Pre and post ELM profiles of a typical Type I ELM crash from the HRTS diagnostic show that the pedestal density collapse on a millisecond time scale is quite different from the temperature collapse, figure 23 [2]. Post ELM measurements between 0 and 1 ms after an ELM-onset show that the pedestal density collapse provokes a rise in the density just outside the separatrix, whereas the T_e -collapse is solely downwards and inside the separatrix. During the next 5ms the density in the SOL disappears due to fast parallel transport, whereas the pedestal density and temperature are recovering from the collapse. As convective and conductive ELM losses are independently determined from the HRTS profiles their ratio can now be quantified at JET [2]. Convective losses are found to not vary significantly and amount to $\sim 5\%$ of the pedestal energy W_{ped} over a large range of pedestal electron collisionality $\nu_e^* < 0.1$ to $\nu_e^* > 0.5$ for H-mode plasmas at low and high triangularity. In contrast, for the same plasmas, conductive losses strongly decrease from $\sim 20\%$ of W_{ped} to 5% of W_{ped} with increasing ν_e^* as shown in figure 24.

3.2 ELM mitigation using active techniques

3.2.1 ELM mitigation using resonant magnetic perturbation

Successful ELM mitigation experiments with external magnetic perturbation fields (EMPFs) induced by the error field correction coils (EFCCs) mounted outside of the vacuum vessel were carried out. The toroidal mode number spectrum of the EFCCs system at JET is limited to $n=1$ and $n=2$ perturbations. Results from these experiments show that the frequency and the amplitude of type-I ELMs can be actively controlled by the application of an $n=1,2$ EMPF generated by the EFCCs [20]. During the application of the $n=1$ field in ITER-relevant configurations and parameters in a wide operational space of plasma triangularity (upper triangularity δ_U up to 0.45), the ELM frequency increased by a factor of 4 (see figure 25). The energy loss per ELM normalized to the total stored energy, $\Delta W_{ELM}/W_{plasma}$, decreases from 7% to below the noise level of the diamagnetic measurement (less than 2%). Such a condition was maintained for durations of 10 times the energy confinement time. It is also shown that ELM mitigation does not depend on the orientation of the $n = 1$ external fields and ELM mitigation is achievable in a wide range of q_{95} (4.8-3.0). The reduction in ELM amplitude, the simultaneous increase in ELM frequency, and a reduction in fast ion losses is observed independent of the phase of the $n=1$ field. A reduction in ELM peak heat fluxes (by roughly the same factor as the increase in ELM frequency) on and in carbon erosion (reduced physical sputtering) of the divertor target plates are observed during the ELM mitigation phase. The application of EMPFs leads to a density pump-out whose origin is not fully understood and that must be compensated by increased gas puffing. Nevertheless, transport analysis using the TRANSP code shows at most a modest reduction of the thermal energy confinement time due

to the density pump-out and, when normalized to the IPB98(y,2) confinement scaling the confinement shows almost no reduction.

3.2.2 ELM mitigation using the vertical stabilisation controller

At JET, first experimental evidence of the application of a rapid varying radial field as ELM pacing mechanism has been obtained [21]. The JET vertical stabilization controller has been modified to allow the application of a user defined voltage pulse (so called kick) at an adjustable frequency which can be synchronised to the ELM event or applied asynchronously. Initial results achieved on deuterium target plasmas with a low density H-mode and low frequency Type-I ELMs (single null magnetic configuration, $I_p=1.9\text{MA}$, $B_T=2.35\text{T}$, $q_95=3.7$, $\kappa=1.72$) show that it has been possible to increase the natural ELM frequency by at least a factor of 5 and to moderate the initial large ELM while keeping the baseline plasma stored energy unchanged (figure 26). Work is presently ongoing at JET to further develop this method and accurately document the effects of the kicks on the edge transport barrier, the ELM structure and the changes in ELM power loadings on the divertor and first wall.

3.2.3 ELM pacing with pellet injection

First results obtained during commissioning of the new high frequency pellet injector at JET [11] confirm the strong potential of pellets to drive and trigger MHD events such as ELMs in JET. Even during L-mode phases, strong pellet driven MHD activity is detected, reaching a magnitude exceeding the one observed at the onset of spontaneous and triggered ELMs during a preceding H-mode phase [22]. It thus appears that there is substantial margin left to reduce the pellet fuelling contribution even further and, hence, minimise a deleterious impact on the plasma confinement.

3.2.4 ELM mitigation by impurity seeding

An alternative way to achieve a substantial reduction of the power load to the target plates during ELMs is the use of extrinsic impurities to increase or replace the intrinsic radiation. This usually leads to a transition to the highly radiating Type-III ELMy H-mode regime. At JET substantial progress has been achieved in extending this regime with N_2 seeding to higher plasma currents up to 3.25MA (figure 27) and, hence, higher densities (up to $1.1 \times 10^{20}\text{m}^{-3}$) [23]. At the highest plasma current the effective charge Z_{eff} is as low as 1.4, mainly due to the increased absolute density and reduced carbon erosion. The advantage of this plasma regime is the tolerable ELM size (the ELM induced transient heat loads onto the outer divertor target are reduced to 2kJm^{-2}) in perspective of ITER (scaled to ITER, Type-III ELMy H-modes are expected to have an energy load of $\sim 0.3\text{MJm}^{-2}$, which is below the technically acceptable limit of 0.5MJm^{-2}), even though at slightly reduced confinement ($\sim 8\text{-}20\%$) as compared to the reference H-mode regime. This scenario could extrapolate to $Q_{DT}=10$ in ITER at 17MA and density approaching n_{GW} , with the increased current compensating for the loss of confinement ($H_{98}(y,2)=0.75$) induced by impurity injection.

3.3 Heat loads on PFCs from disruptions

Recent infra-red measurements of heat loads on PFCs using the JET wide angle viewing system during vertical displacement events, density limit disruptions and radiation limit disruptions indicate that up to 60% of the thermal energy is released onto the upper dump plate (starting from the thermal quench) [24], in accordance with previous observations indicating that only 10-50% of that energy is deposited on the divertor targets [25]. It is found that for density limit and radiative limit disruptions the timescale for energy deposition at the upper wall during the thermal quench is substantially longer (by a factor 3-8) than the core plasma collapse time. For vertical displacement events, this ratio is smaller (a factor 1.5-4).

The heat load profiles measured on the upper dump plate during the thermal quench show substantial broadening of the power footprint in agreement with previous observations made on the divertor. With a SOL power decay length of 30mm determined 3.2ms after the thermal quench, a broadening by a factor 3 is found compared to the value determined few ms before the thermal quench. Despite this broadening near the separatrix contact point with the upper wall, shadowing of the power fluxes to remote elements in the vacuum vessel by the JET inner wall and outer limiters leads to noticeable steeper gradient of the power flux in the far scrape off layer. This provides a guideline to be taken into account for the optimisation of the detailed design of the main wall plasma facing components in ITER.

Measurements from a new fast bolometer indicate that most of the energy is radiated during the current quench and corresponds to about 30-40% of the total available magnetic energy.

3.4 Material migration and fuel retention

The physical mechanisms underlying material erosion, long and short range migration and re-deposition within the present full carbon walls in JET have been addressed with the particular aim to prepare for future comparisons with results from the foreseen ITER-like wall [9]. These studies have benefited from improved diagnostics and dedicated pulse sequences. Spatial distribution and layer characteristics have been identified with dedicated slow plasma sweeps and spatially resolved hydrocarbon spectroscopy and Quartz microbalance deposition detectors which have been placed around the JET divertor. The main results can be summarised as follows [26]: (i) Carbon is mainly released from first wall and deposited in the inner divertor. The magnetic configuration is the main factor which determines the deposition pattern in first place, e.g. the private flux region turns from net deposition to erosion when the configuration changes from strike points on the vertical to strike points on the horizontal target; (ii) The deposited carbon undergoes further transport inside the divertor by a stepwise process induced by new magnetic configurations which lead to enhanced re-erosion of freshly deposited layers; (iii) A strongly nonlinear increase of the local carbon release and migration inside the divertor with ELM size is found such that a few large type I ELMs lead to a stronger migration than many small ELMs. These observations can explain the large carbon deposition and tritium retention on remote areas (louvers) in the JET DTE1 experiments in 1997. They show also that the dynamics of carbon transport is a specific carbon property related to the chemical sputtering probability, which is then coupled with the deposition and fast disintegration of carbon layers. Such effects are not expected for metallic layers such as beryllium that will be used in the main chamber of ITER. Moreover, the main difference found between carbon and beryllium (from beryllium evaporation) migration in JET is the fact that beryllium remains close to the location of the inner strike-point. The overall particle balance has been studied in JET in a series of repetitive and identical discharges with an overall accuracy of about 1.2%. The particle retention behaviour has been analysed [27] for L-modes and H-modes (Type III and Type I ELMs with energy ~100kJ) discharges in the same magnetic configuration ($I_p=2\text{MA}$, $B_T=2.4\text{T}$, average particle density $\langle n_e \rangle = 4.5 \times 10^{19} \text{m}^{-3}$, gas injection rate $1.8 \times 10^{22} \text{Ds}^{-1}$). For all the experiments, active pumping was ensured by the divertor cryopump only (all main chamber pumps closed) and its regeneration (to liquid nitrogen temperature) before and after the series (~at least 1/2 hour after the last pulse) thus allowing a direct measure of the long term retention. In this analysis the short term retention is assumed to be recovered in between pulses. Co-deposition is found to dominate the long term retention and it is also expected to be the case for beryllium within the future ITER-like wall in JET and in ITER. The overall results for the three different scenarios investigated in JET are summarised in table 1 [27]. Increase of the long term retention is observed from L mode to Type-I ELMy H-mode and is associated to the increase of the recycling flux and the carbon flux resulting from erosion in the main chamber, thus

confirming the strong concerns about fuel retention in a carbon clad tokamak and indicating that full carbon in all PFCs in ITER would dramatically limit operation to a few tens of DT discharges at full performance before reaching the safety limit of 700g of retained tritium.

Pulse type	Injection rate per pulse (Ds^{-1})	Cumulated heating phase (s)	Long term retention (Ds^{-1}) (heating phase)	Divertor phase (s)	Long term retention (Ds^{-1}) (divertor phase)
L-mode	$\sim 1.8 \times 10^{22}$	81	2.04×10^{21}	126	1.27×10^{21}
H-mode Type III	$\sim 1.7 \times 10^{22}$	72	2.40×10^{21}	126	1.37×10^{21}
H-mode Type I	$\sim 1.7 \times 10^{22}$	32	2.83×10^{21}	50	1.7×10^{21}

Table 1 Particle injection rate during the heating phase (second column), cumulated heating time for the series of discharges (third column), averaged long term retention rate evaluated over the cumulated heating time (fourth column), cumulated divertor phase for the series of discharges (fifth column) and averaged long term retention rate evaluated over the cumulated divertor time (last column) for the three series of experiments in L mode, Type III and Type I ELMy H-mode.

4 Toroidal field ripple effects on H-modes and implications for ITER

In all tokamak devices, the finite number and toroidal extension of the toroidal magnetic field coils causes a periodic variation of the TF from its nominal value, called the TF ripple defined as $\delta_{BT} = (B_{\max} - B_{\min}) / (B_{\max} + B_{\min})$. Uniquely to JET, it is possible to vary the TF ripple amplitude by independently powering the 16 odd and 16 even numbered coils. The TF ripple can thereby be increased from its nominal value at the separatrix (outboard mid-plane) $\delta_{BT} \sim 0.08\%$ up to $\delta_{BT} \sim 3\%$. A series of experiments has recently been conducted at JET aiming at quantifying, for a range of plasma conditions, the impact of ripple on H-mode confinement and attempting to identify an acceptable maximum ripple for ITER [28]. To begin with, an H-mode reference discharge with Type I ELMs at δ_{BT} of 0.08% was first established and then the ripple increased in steps (0.3%, 0.5% and 0.7%) from pulse to pulse to a maximum of 1%. Most studies were carried out at plasma current $I_p = 2.6 \text{ MA} / B_T = 2.2 \text{ T}$ ($q_{95} \sim 2.9$) at low δ (~ 0.22) with NB co-current injection.

4.1 Behaviour of plasma confinement and rotation with ripple

Increasing the toroidal field ripple in plasmas with no gas fuelling in the H-mode phase has a detrimental effect on plasma density and confinement (figures 28 and 29), especially at low pedestal collisionality [28]. Specifically, increasing δ_{BT} from the standard 0.08% level to 1% causes a reduction of the confinement enhancement factor, $H_{98}(y,2)$, of $\sim 20\%$ with most of the density loss already observed at $\delta_{BT} = 0.5\%$. Within the measurement uncertainty, the deterioration of plasma confinement with ripple magnitude is continuous (although not necessarily linearly proportional to δ_{BT}). The very non-linear dependence of Q_{DT} on the confinement enhancement factor H_{98} ($\sim H_{98}^{3.3}$) implies that even “small” reductions of the plasma confinement would result in a reduction of the fusion power not acceptable for ITER. Moreover, given that the fusion power output is proportional to the density (at constant temperature), the impact of density pump out on Q_{DT} is even more severe than what is deduced from the reduction of the $H_{98}(y,2)$ factor. Even for small TF ripple amplitudes of $\delta_{BT} \sim 0.5\%$ the JET plasma rotation is significantly reduced compared to normal levels. In the discharges with $\delta_{BT} \sim 0.5\%$ a counter current torque was found in the order of 20-30% of that supplied by the NBI system in co-current direction and for $\delta_{BT} \sim 1\%$ an area of counter rotation develops at the edge of the plasma, while the core keeps its co-rotation [29]. The dominant mechanism that drives the observed counter rotation in the discharges with a large $\delta_{BT} > 0.5\%$ can be associated with banana orbit diffusion of trapped energetic ions (by NBI). However, calculations with the ASCOT code of the induced torque due to these losses do not fully explain the observations. The edge rotation in the presence of a large TF ripple appears to depend on the local ion temperature, suggesting that other ion losses, possibly those of

thermal ions, may be involved. The effect of TF ripple on thermal ions has so far not been included in the ASCOT calculations.

4.2 Effect of TF ripple on ELMs

The analysis of the JET data shows that toroidal field ripple affects ELM frequency and size [28]. With increased ripple from 0.08% to 0.5% the Type I ELM frequency almost doubles, going from ~12Hz to ~20Hz. With ripple increased further to 0.7% and finally 1%, ELMs become irregular, with Type I, Type III and long ELM-free phases, in spite of the fact that the power across the separatrix remains approximately constant. Moreover, the data indicate that Type I ELM size is reduced, for 1% ripple, by about a factor of two and that the ELM losses seem to become more convective. Although a reduction of the ELM size may look attractive for ITER, the JET results show that this would come at the price of significant confinement deterioration. Therefore, the JET results suggests that $\delta_{BT} < 0.5\%$ is required in ITER in order to achieve the $Q_{DT}=10$ goal and reduce the uncertainty on confinement extrapolation as well as the impact on plasma rotation.

4.3 TF ripple impact on ITB formation and strength

Another important issue associated with the TF ripple is its effect on the formation and strength of ITB. Dedicated experiments have shown that, although the ITB trigger was unaffected (figure 30), the further development of the ITB may be degraded due to larger TF ripple [30, 31]. The TF ripple reduces the toroidal rotation and modifies the toroidal rotation profile (figure 31) while no effect on the poloidal rotation has been observed. It suggests that stronger barriers form in the presence of a larger rotational shear. The ITB triggering was unaffected by the changes in rotational shear and, in these experiments, this mechanism may be predominantly determined by the detailed shape of the safety factor profile.

5 Stability and transport

5.1 Resistive wall mode stability up to the no-wall limit

Plasma operation at high β_N (such as required for AT scenarios) is often limited by pressure-driven MHD instabilities. Although the presence of a conducting wall increases this β -limit, it is important to know the ideal no-wall β -limit as resistive wall modes (RWM) can occur above this level. It is known that the Resonant Field Amplification (RFA) of an externally applied helical magnetic field is significantly enhanced when a plasma exceeds the ideal no-wall stability limit [32], suggesting that this might be used for stability probing. Measurements of the plasma response to an applied AC $n=1$ or $n=2$ helical magnetic fields (produced by EFCCs) in high- β scenarios in JET show that the RFA threshold on JET decreases with increasing q_{min} , as predicted by modelling [6]. This new diagnostic also allows estimation of the duration of the plasma sustainment over the RFA threshold. Values of β_N up to 70% above the measured RFA threshold have been transiently obtained, which is significantly more than the 20% expected from the relationship between no-wall limit and RFA threshold. The possibility of RFA well below the no-wall limit and the condition under which this could happen have been investigated with linear ideal MHD stability codes and appear to be linked to marginally stable current driven modes.

5.2 Momentum, ion and electron heat transport

Understanding the physics of momentum transport is one of the urgent physics tasks in view of predicting the level of rotation in ITER. A rotation database covering more than 600 JET discharges shows that the effective Prandtl number is substantially below one in the JET core plasma, $P_{r,eff} = \chi_{\phi,eff} / \chi_{i,eff} \sim 0.1-0.4$ [33], in apparent contradiction with Ion Temperature Gradient (ITG) based theories and gyro-kinetic calculations reporting ‘purely diffusive’ Prandtl

numbers $P_r = \chi_\phi / \chi_i \sim 1$. However, recent developments in theory predict a sizeable inward momentum pinch [34] which could resolve the discrepancy as the inward pinch results in $P_{r,eff}$ being smaller than P_r . Moreover, experiments at JET aiming at decoupling power input and torque included modulation at 6.25/8.33Hz using NBI to create a periodic perturbation in the toroidal rotation velocity (see figure 32) and, hence, determine the diffusive and convective momentum transport [35]. Novel transport analysis for these experiments shows the magnitude and profile shape of the momentum diffusivity is similar to those of the ion heat diffusivity. Also, a significant inward momentum pinch, up to 20m/s, is found. An inward momentum pinch may result in a centrally peaked toroidal velocity profile in ITER, even in the absence of any external core momentum source. A related issue is the role of rotation on plasma turbulence and confinement. The existence of a threshold in the ion temperature inverse gradient length R/L_{Ti} ($=R|\nabla T_i|/T_i$, with R the torus major radius) for the onset of ITG modes is experimentally confirmed in JET low rotation plasmas [36] (see figure 33) and its value found in close agreement with linear GS2 gyro-kinetic calculations. The stiffness level is high and keeps R/L_{Ti} close to the linear threshold. This finding is not in agreement with the non-linear GS2 calculations which yield significant higher R/L_{Ti} than the linear threshold. Electrons are generally found less stiff than ions [37]. Comparisons of plasmas with different values of toroidal rotation indicate a significant increase in R/L_{Ti} in rotating plasmas. Various observations allow to conclude that such increase is mainly due to a decrease of the stiffness level with increasing rotation, rather than to a mere up-shift of the threshold, as commonly predicted by theory. This finding has implications on the interpretation of present day experimental results on the effect of rotation on confinement as well as on extrapolations to ITER/DEMO.

5.3 Fast ions studies

Studies of various plasma scenarios based on the synergy of a unique set of diagnostics for confined and lost particle measurements (γ -ray diagnostics, thin foil Faraday Cup array and a scintillator probe) [38] show that a significant redistribution of fast ions happens during the change in q profile from strongly shear-reversed to monotonic (see figure 34). Also, significant changes in the losses of ICRH accelerated protons are observed during confinement transitions: after an L-H transition an abrupt decrease in the ICRH proton losses is observed; in plasmas with an ITB, losses of ICRH-accelerated ions increase as the barrier forms. Furthermore, investigations of the response of ions to MHD modes show a dependence of the loss intensity on the MHD mode amplitude.

6 Plasma heating studies and systems development

Plasma heating optimisation studies in support of the ITER scenarios at JET include the coupling of ICRF/LH power in ELMy H-mode at large antenna-plasma distances [39]. D_2 gas puffing in the plasma edge has been applied on H-Mode plasmas with high- δ , significant differences in ELM behaviour and recycling and a radial outer gap of up to 14cm. This has led to a significant improvement of the ICRF antenna loading (up to a factor of 6) allowing to couple up to 8MW of ICRF power during ELMs (figure 35). LH power coupling at large gaps has been optimised, delivering 3MW to the plasma during 8s in a stationary way, at a plasma-separatrix/launcher distance of up to 15cm [40]. Three new improvements have recently been made to the JET ICRF antennae to both increase coupled power density and match through rapid coupling variations during ELM's [41]; both of which are key developments for the future design of the ITER ICRF antenna. Firstly, 3dB couplers were fitted to two antennae in 2004/5. Secondly, a new ITER-like antenna (ILA) was installed during 2007 to couple an ITER-relevant power density ($8MW/m^2$) using a close-packed array of straps, with ELM tolerance incorporated using an internal (in-vacuum) conjugate-T junction with each strap fed

through in-vessel matching capacitors from a common vacuum transmission line. Thirdly, an externally-mounted conjugate-T system has been installed on two antennae during the 2007. Initial operation of the JET ILA has already shown that it is feasible to match such antennas to a variety of JET plasmas [41].

7 Outlook

JET is presently in the middle of a large enhancement programme [11] that includes the installation of a beryllium wall and a tungsten divertor [9], the upgrade of the neutral beam power from about 24MW/10s up to 36MW/20s, the upgrade of the vertical stability control, the installation of a high frequency pellet injector for fuelling and ELM control and about 20 new diagnostics. Some of these enhancements will come to fruition during the 2008 and 2009 Campaigns. The present planning foresees a shutdown from the middle of 2009 to the middle of 2010 for the installation of the new ITER-like wall and the neutral beam enhancement, followed by a 26 weeks restart phase during which the new JET wall will start to provide important information for ITER. The full exploitation of the enhancements requires the extension of JET until 2014, including a DT experiment.

Acknowledgement

This work was carried out within the framework of the European Fusion Development Agreement. The views and opinions expressed herein do not necessarily reflect those of the European Commission. The results presented in this paper have been obtained through the collective effort of all the JET-EFDA contributors. The authors are particularly thankful to M. L. Watkins, G. Saibene, P. Lang, T. Loarer, E. Joffrin, F. Rimini, V. Pericoli, R. Koslowski, V. Naulin, T. Tala, W. Fundamenski, S. Brezinsek, T. Eich, J. Ongena, M. Mayoral, A. Murari, E. de La Luna, D. Mazon, B. Gonçalves, D. McDonald, P. Lomas, P. Mantica, J. Mailloux, P.C. de Vries and M.N.A. Beurskens.

References

- [1] ITER Physics Basis, Nucl. Fusion 39 (1999) 2368
- [2] BEURSKENS, M.N.A. et al., paper EX/P3-4, this conference
- [3] MCDONALD, D. C., et al., to appear in Plasma Phys. Control. Fusion (2008)
- [4] JOFFRIN, E. et al., paper EX/1-4Ra
- [5] RIMINI, F. G. et al., paper EX/1-2, this conference
- [6] GRYAZNEVICH, M. P., et al., submitted to Plasma Phys. Control. Fusion 2008
- [7] LITAUDON, X. et al., Plasma Phys. Control. Fusion 49 (2007) B529
- [8] BEURSKENS, M.N.A. et al., Nucl. Fusion 48 (2008) 095004
- [9] PAMELA, J. et al., J. Nucl. Mater. 363-365 (2007) 1
- [10] PIRONTI, A. et al., Proc. 34th EPS Conf. on Plasma Phys. Control. Fusion (Warsaw, 2007)
- [11] PAMÉLA, J. et al., Fusion Engineering and Design 82 (2007) 590
- [12] KOSLOWSKI, H.R. et al, Proc. 34th EPS Conf. on Plasma Physics (Warsaw, 2007) P5.135
- [13] SIPS, A. C. C. et al., paper IT/2-2, this conference
- [14] PITTS, R. A. et al., Proc. of the 18th PSI, (26th-30th May 2008) Toledo, Spain
- [15] FUNDAMENSKI, W. et al., J. Nucl. Mater. 363-365 (2007) 319
- [16] FUNDAMENSKI, W., et al., paper EX/4-3Ra, this conference
- [17] EICH, T et al., paper EX/4-3Rb, this conference
- [18] LOARTE, A., et al., paper IT/P6-13 this conference
- [19] EICH, T., et al, Phys. Rev. Letters 91 (2003) 195003
- [20] LIANG, Y. et al., paper EX/4-2, this conference
- [21] SARTORI, F. et al., Proc. 35th EPS Conf. on Plasma Phys. Control. Fusion (Crete, 2008)
- [22] LANG, P. et al., paper EX/4-5, this conference
- [23] RAPP, J. et al., paper EX/4-4Rb, this conference

- [24] ARNOUX, G. et al., paper EX/7-2Ra, this conference
- [25] PALEY, J. et al., J. Nucl. Mater., 337-339 (2005) 702-706
- [26] BREZINSEK, S., et al., submitted to Plasma Phys. Control. Fusion (2008)
- [27] LOARER, T. et al., Proc. of 18th PSI conference, 26-28 May 2008, Toledo, Spain
- [28] SAIBENE, G. et al., paper EX/2-1, this conference
- [29] de VRIES, P.C., et al., Nucl. Fusion 48 (2008) 035007
- [30] de VRIES, P.C., et al., Plasma Phys. Control. Fusion 50 (2008) 065008
- [31] de VRIES, P.C., et al., paper EX/8-3, this conference
- [32] GAROFALO, A., et al., Phys. Plasmas 9 (2002)1997
- [33] de VRIES, P.C., et al., Plasma Phys. Control. Fusion **48**, 1693 (2008)
- [34] PEETERS, A.G., et al., Phys. Rev. Lett. **98**, 265003 (2007)
- [35] TALA, T., et al., paper EX/3-3, this conference
- [36] MANTICA, P. et al., paper EX/2-4, this conference
- [37] RYTER, F. Et al., paper EX/P5-19, this conference
- [38] KIPTILY, V. G. et al., paper EX/P8-8, this conference
- [39] ONGENA, J., et al., paper EX/P6-33, this conference
- [40] GONICHE, M., et al., paper EX/P6-22, this conference
- [41] NIGHTINGALE, M. et al., paper FT/4-5Ra, this conference

Figures

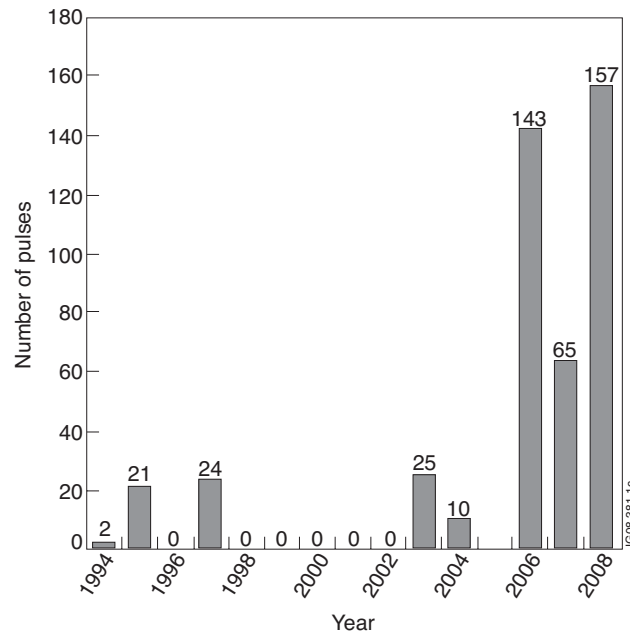


Figure 1: Number of JET pulses with injected neutral beam power above 20 MW

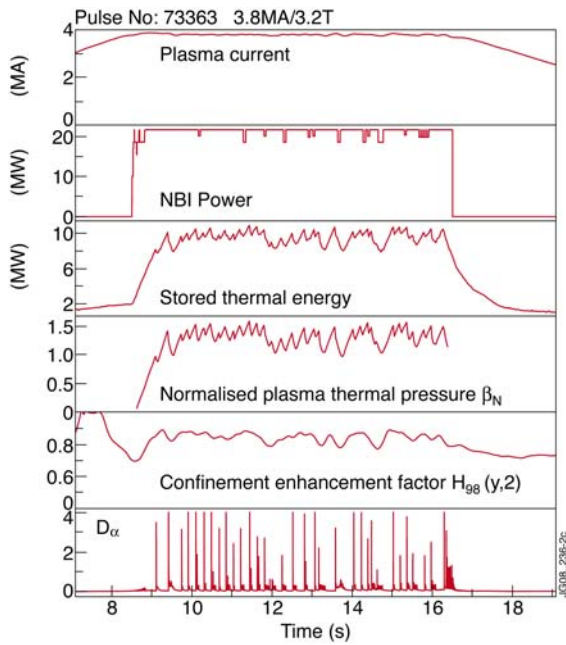


Figure 2: Time traces for the plasma discharge #73369 at $I_p/B_T = 3.8\text{MA}/3.2\text{T}$

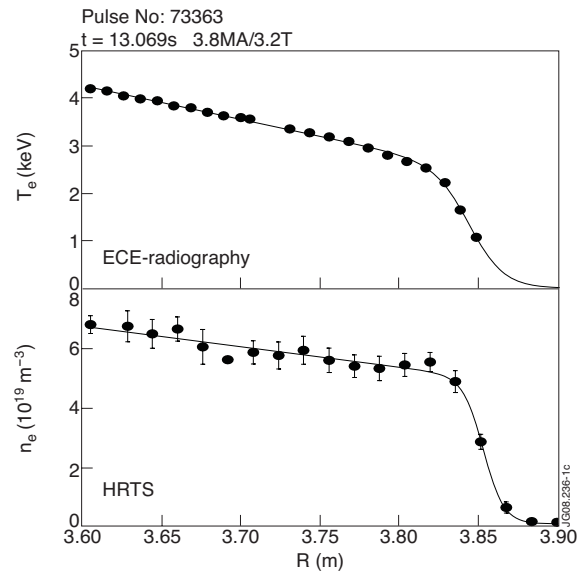


Figure 3: Highly resolved profiles of electron temperature and density for plasma discharge #73369.

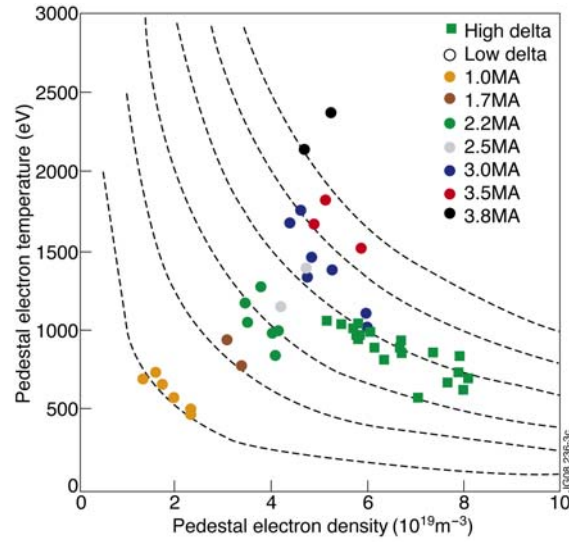


Figure 4: Pedestal T_e and n_e diagram for ELMy H-modes at low ($\delta \sim 0.25$) and high ($\delta \sim 0.4$) triangularity and various plasma currents (1MA-3.8MA, $q_{95}=3$ and 3.6).

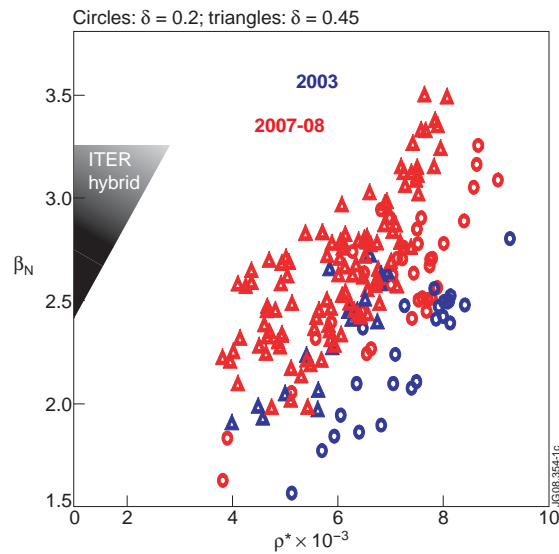


Figure 5: Recent extension of the hybrid scenario in JET in β_N and ρ^*_i for $\delta=0.2$ (circles) and $\delta=0.45$ (triangles).

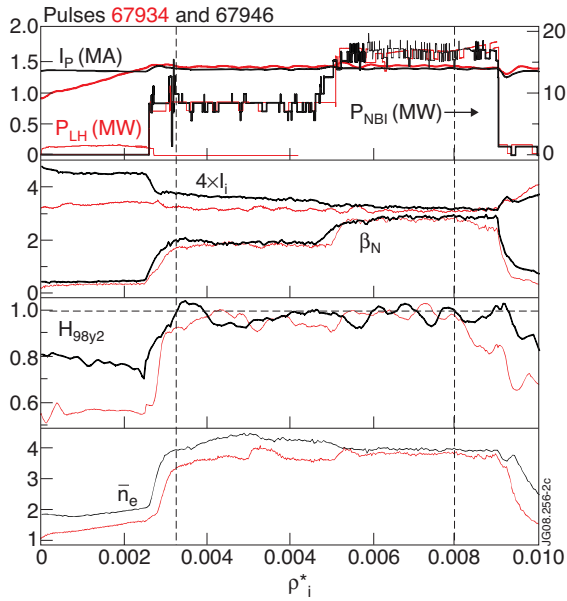


Figure 6: Time traces for a typical JET hybrid scenario (red) overlaid with those of a comparative H-mode (black) without initial q profile tailoring and shifted in time by 15.5s. No difference is observed at 12s between the two discharges even though the hybrid is initially starting with a very different q profile (at 5s). Dotted lines indicate the time of the q profiles shown in figure 9.

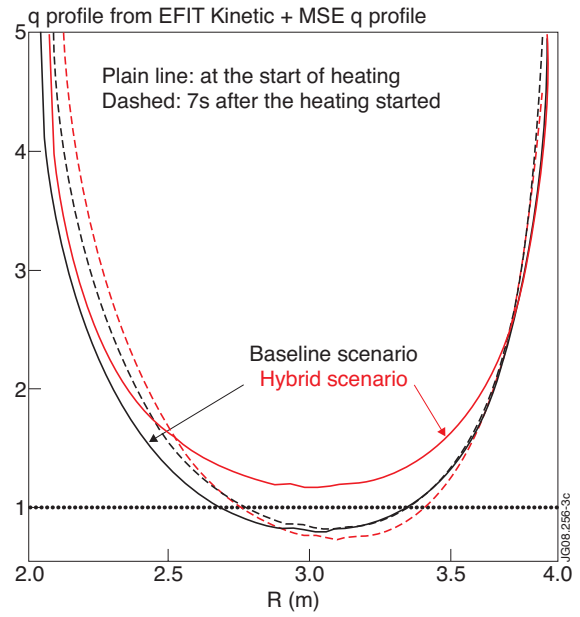


Figure 7: Comparison of the q profiles of the hybrid and H-mode scenarios. After 7s of heating (dashed lines), the q profiles are identical within the error bars of the reconstruction.

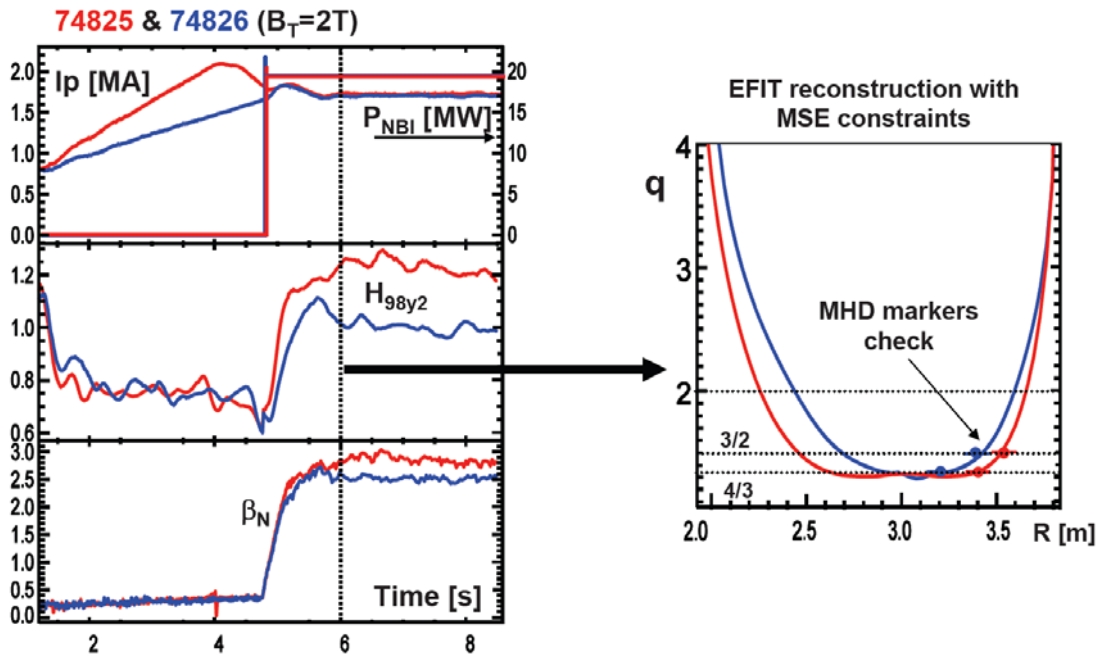


Figure 8: Comparison of two hybrid discharges with (#74825) and without (#74826) strong current ramp-up and then ramp down. The picture on the right shows a significantly broader q profile for discharge #74825.

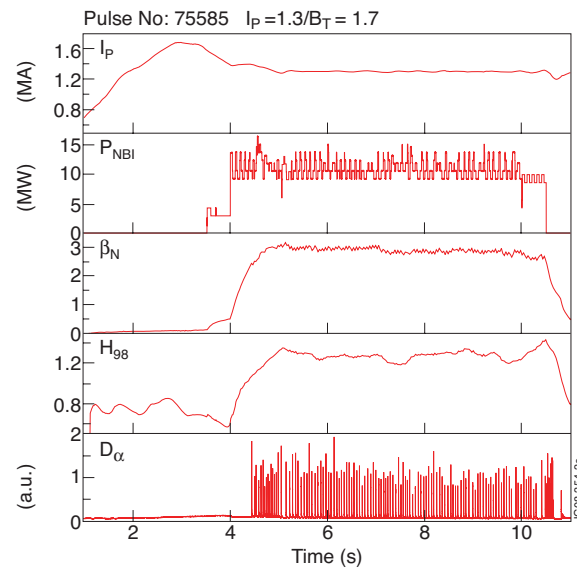


Figure 9: Time traces for the hybrid scenario discharge #75585 at $\delta=0.4$.

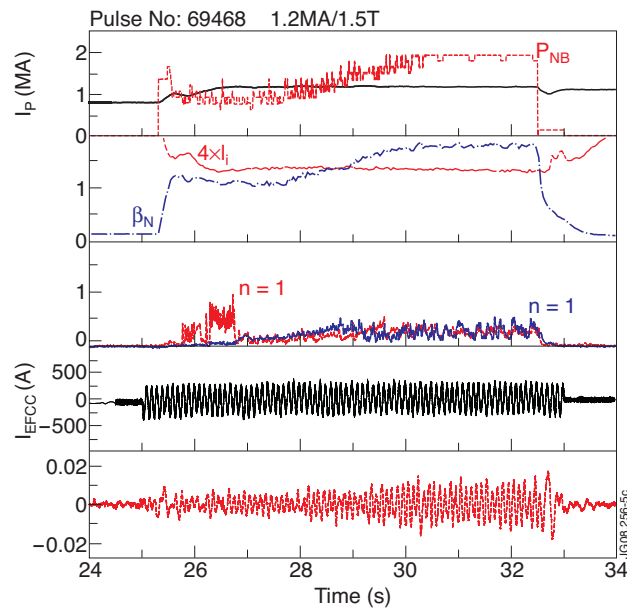


Figure 10: MHD spectroscopy applied to the scenario with $q \geq 1$ reaching $\beta_N=3.6$. Resonant field amplification is observed at around 29s at the minimum of the ratio: RFA amplitude / β_N .

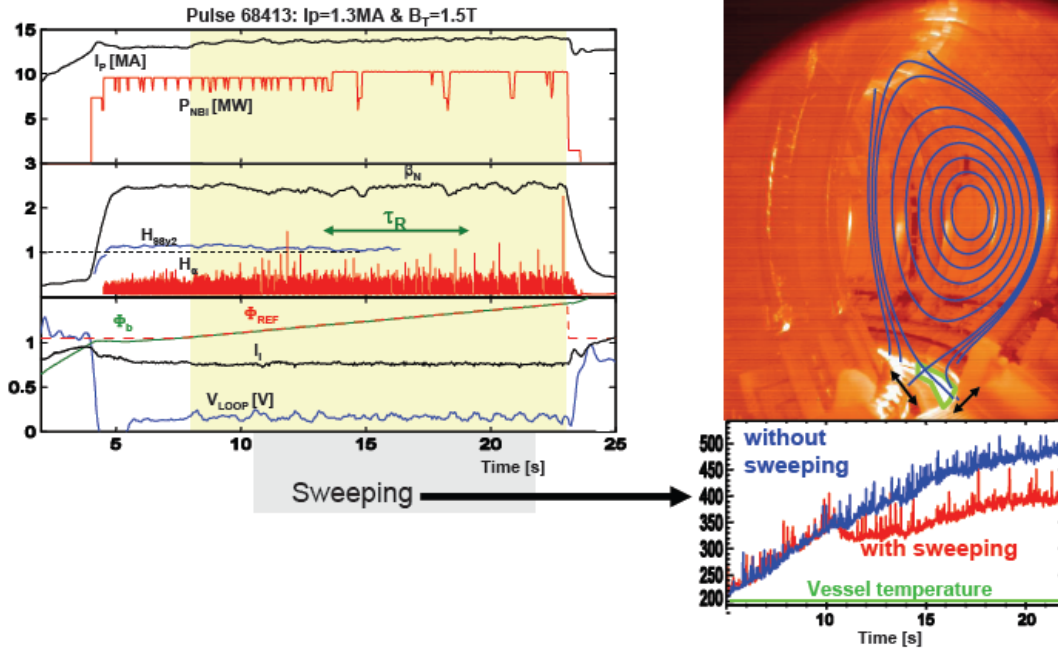


Figure 11: Typical 20s pulse with boundary flux control and strike points sweeping. The main non-inductive current components are the bootstrap current (35% of total current) and the neutral beam driven current (25%). The control window is indicated by the shaded area. The picture on the right shows the difference in divertor tile temperature with and without sweeping as measured with the wide-angle infrared camera (providing the inside view of the JET vessel on top panel).

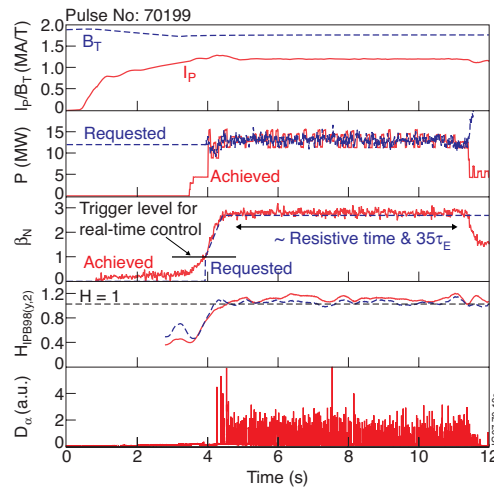


Figure 12: Time evolution of a typical high β_N pulse showing plasma current and magnetic field: requested and achieved NBI power; requested and achieved β_N ; $H_{98}(y,2)$ and D_α .

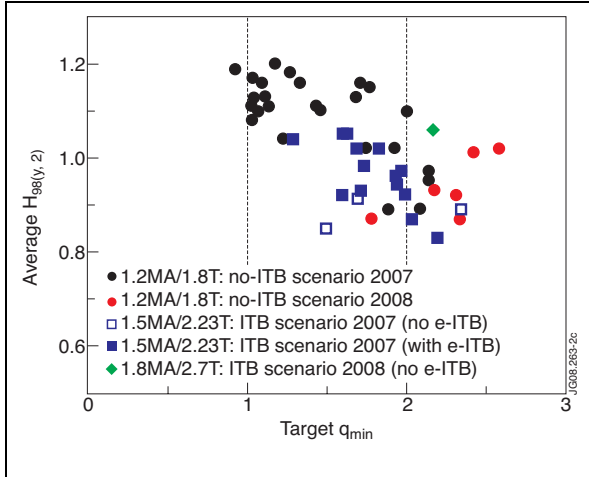


Figure 13: Normalised confinement, $H_{98}(y,2)$, versus target q_{min} for both ITB and no-ITB cases.

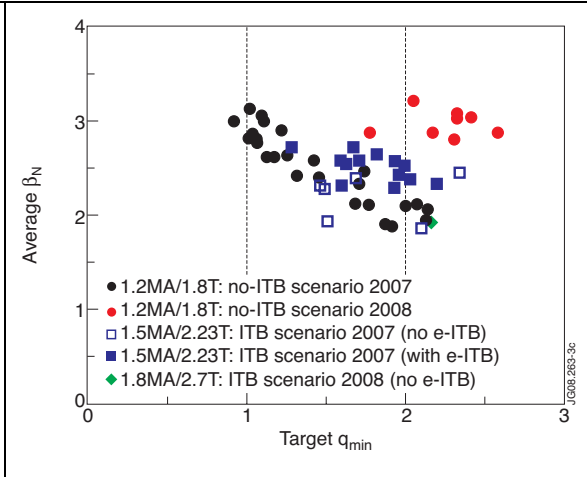


Figure 14: Normalised β versus target q_{min} for both ITB and no-ITB cases.

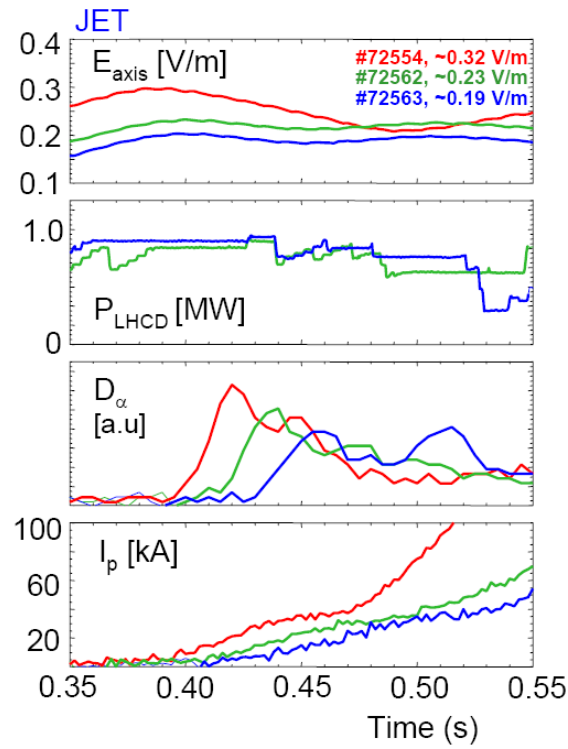


Figure 15: Low voltage start up experiments in JET. Shown from top to bottom are the electric field on axis, the LHCD power used, the measurements of the D_α emission in the main chamber, and the plasma current evolution. No pre-ionisation is observed (no D_α emission) before the plasma current rises.

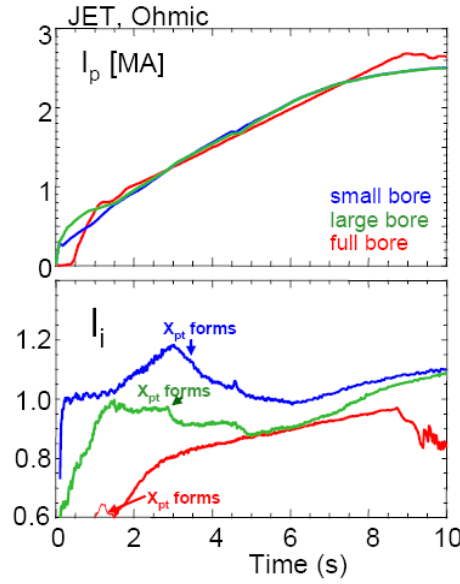


Figure 16: Evolution of $I_i(3)$ for ohmic current rise phases at JET. The evolution for the originally envisaged small bore start up for ITER is indicated in blue. Full bore ramp up discharges for both devices are indicated in red. The green curve for JET is a large bore outer limiter case with somewhat later X-point formation compared to the red discharge.

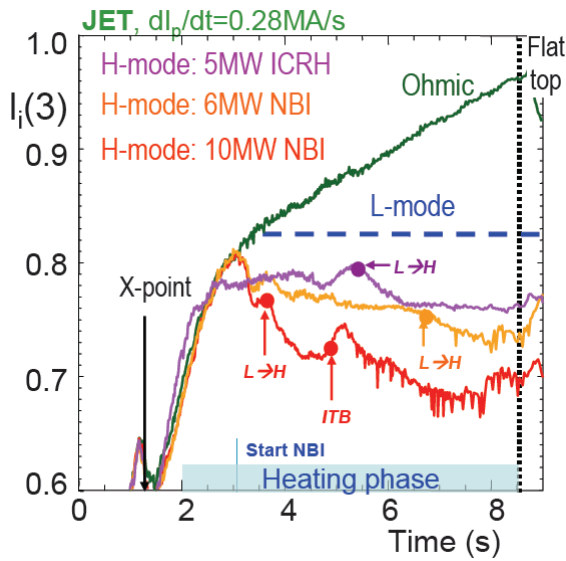


Figure 17: Heated current rise phases in JET. A reduction of $I_i(3)$ with heating during the current rise is observed. A current rise for $dI_p/dt=0.28\text{MA/s}$ is used, experiments in L-mode with moderate heating (3-5MW) usually achieve $I_i(3) \sim 0.85$, indicated by the blue dotted

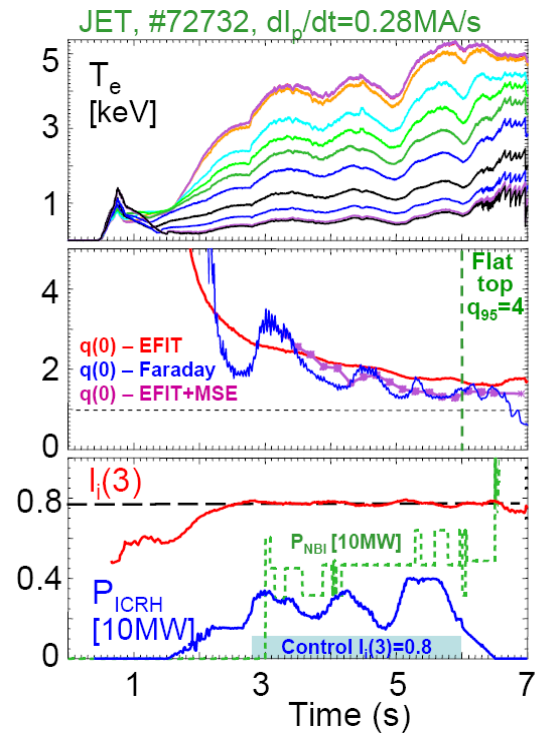


Figure 18: JET discharge ramping to $q_{95}=4$ at $dI_p/dt=0.28\text{MA/s}$. Shown is a control of $I_i(3)=0.8$ with ICRH, giving $q(0)>1$ at 6s. The level evolution of NBI power to give the same $I_i(3)=0.8$ (previous pulses) is indicated. Shown from top to bottom are the

line for reference. Transitions to H-mode and phases with an internal transport barrier (ITB) are indicated.

electron temperature at various radii, the evolution of the $q(0)$ using different reconstruction methods, and the $I_i(3)$ evolution compared to the set point of 0.8, together with the ICRH and NBI power used.

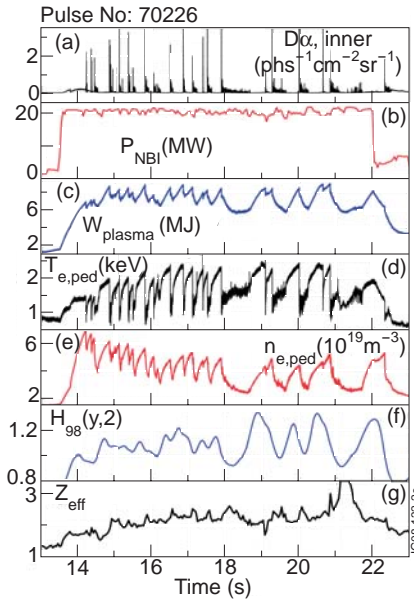


Figure 19: (a-g) Selected plasma signals for a 3.0MA H-mode discharge with gas fuelling $\Gamma_{\text{gas}} = 0$.

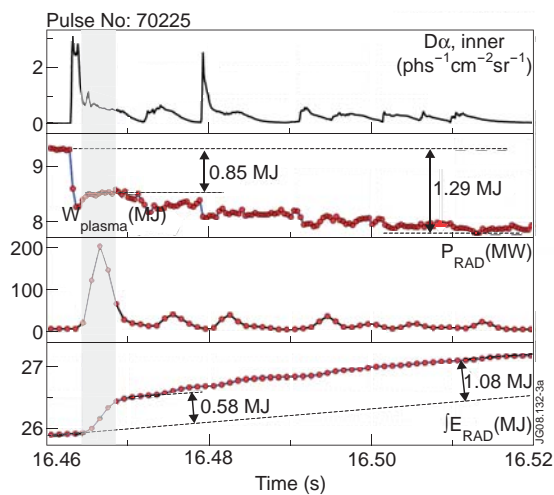


Figure 20a: Energy balance during a single large ELM.

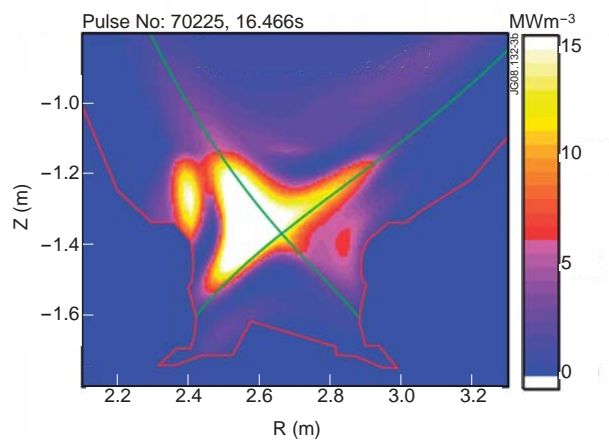


Figure 20b: Tomographic reconstruction of the ELM radiation distribution averaged over shaded region in figure 21a. The picture shows a strong in-out asymmetry in ELM induced

radiation, probably due to layers on inner targets and preferential inboard deposition of ELM energy. For the present case the amount of energy radiated during/after the ELM as a fraction of the ELM energy is found to be ~ 0.69 .

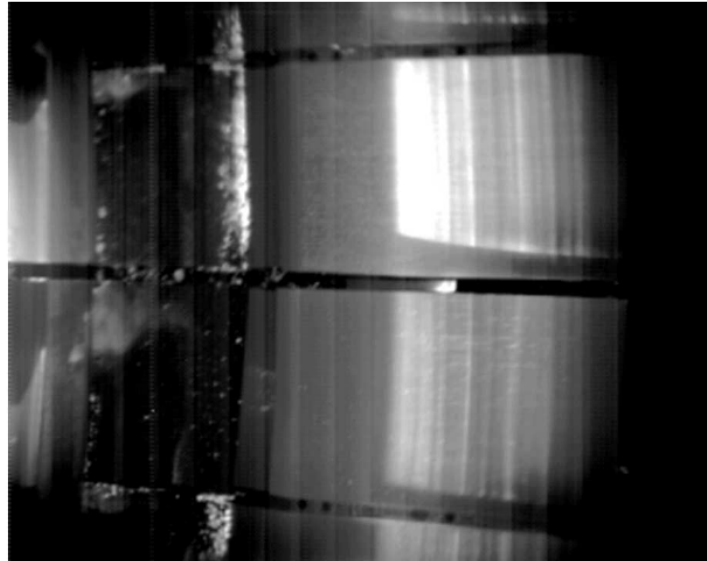


Figure 21: Raw picture from the new divertor infra-red camera at JET which combines a high temporal resolution of $85\mu\text{s}$ with high spatial target resolution of 1.7mm for the outboard and 5.3mm for the inboard targets necessary to study the ELM power load evolution in detail. Here, the power deposition at the outer strike line during an ELM resembles the footprints of single filaments, particularly obvious in the far scrape-off layer. The footprints correspond to a quasi mode number of 6-8 here. Note that the inboard strike line is located on the vertical part of the inboard tile which is hidden with respect to the infra red viewing geometry.

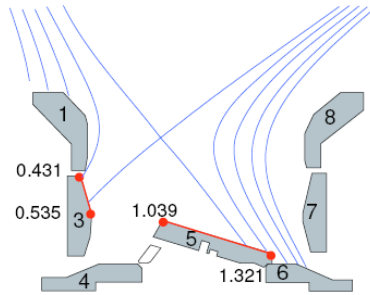


Figure 22a: JET divertor target geometry and magnetic field reconstruction for discharge #73920. The top window viewing position of the divertor IR camera implies that the spatial coverage is quite different for inner and outer targets: the entire surface of tile #5 is well observed but only the upper part of tile #3. Power load calculations are performed for the surfaces marked in red. Decimal numbers indicate the target coordinate s consistent with the indications in figure 22b

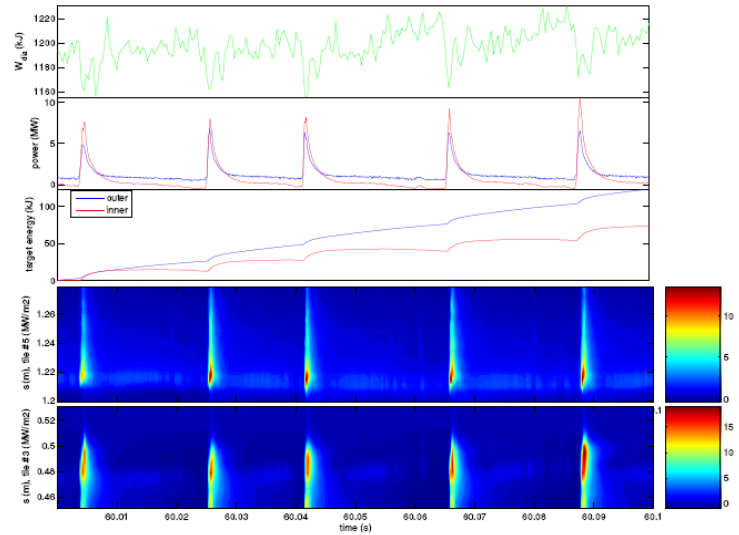


Figure 22b: From top to bottom: time evolution of the plasma stored energy, the inner and outer target power fluxes and energy for a restricted time window of discharge #73920.

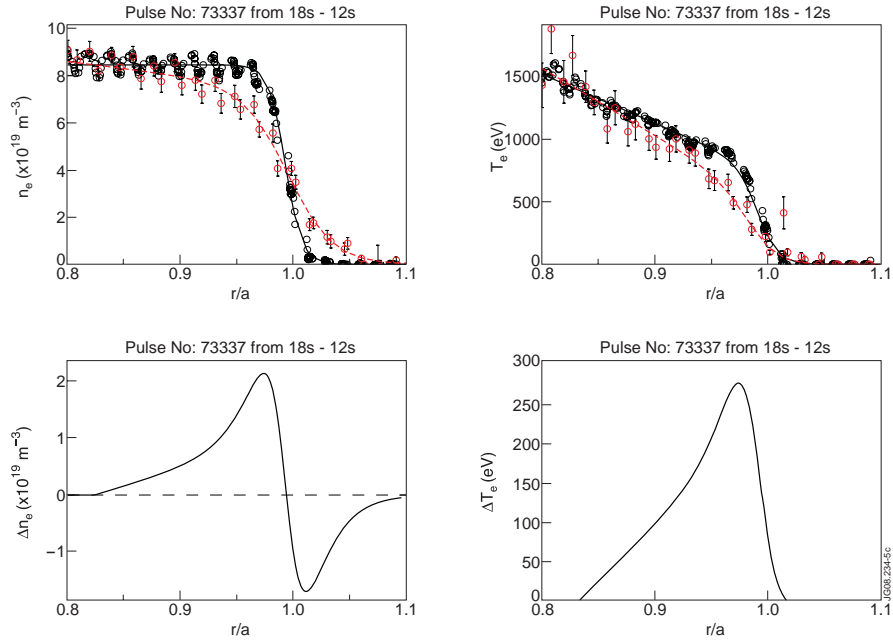


Figure 23: (a) and (b) Pre-ELM (black) and Post-ELM (red) density and temperature profiles from HRTS of a high triangularity ELMy H-mode. (c) and (d) Particle and temperature loss due to the ELM event. Pre-ELM profiles selected in $-1\text{ms} < t_{\text{elm}} < 0\text{ms}$ and post ELM profiles selected between $0.1 \text{ ms} < t_{\text{elm}} < 1 \text{ ms}$.

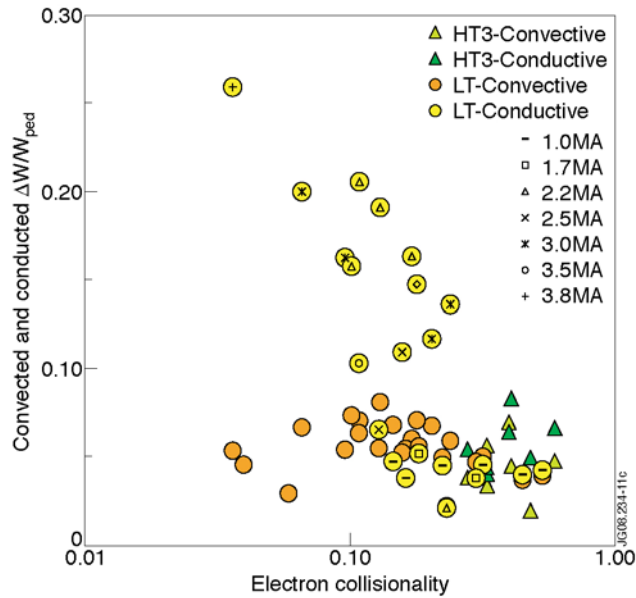


Figure 24: Fractional Convective and conductive ELM energy losses versus electron collisionality ν^*_e for H-mode plasmas at low (LT) and high (HT3) triangularity and different plasma currents.

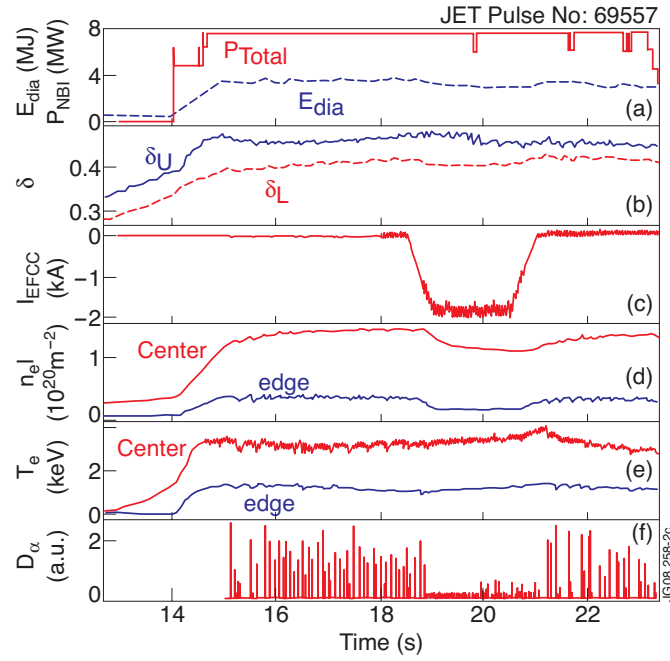


Figure 25: (a)-(f) Overview on a typical ELM control experiment using error field correction coils (EFCCs) in a high triangularity JET plasma.

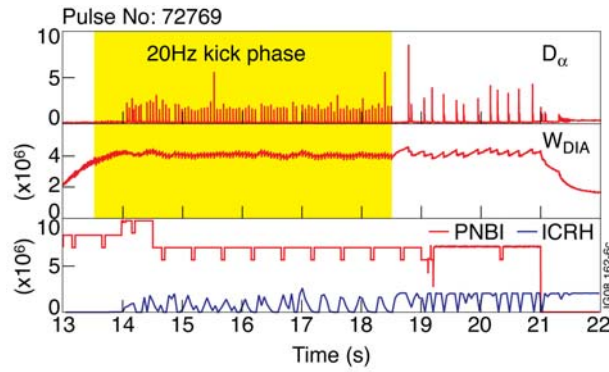


Figure 26: Demonstration that magnetic ELM pacing using vertical kicks to the plasma does not strongly affect the plasma baseline stored energy.

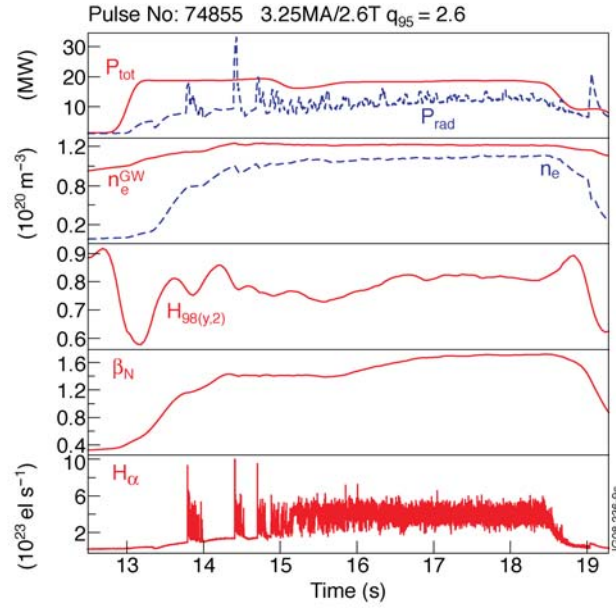


Figure 27: Overview of 3.25MA/2.6T type-III ELMy H-modes at JET.

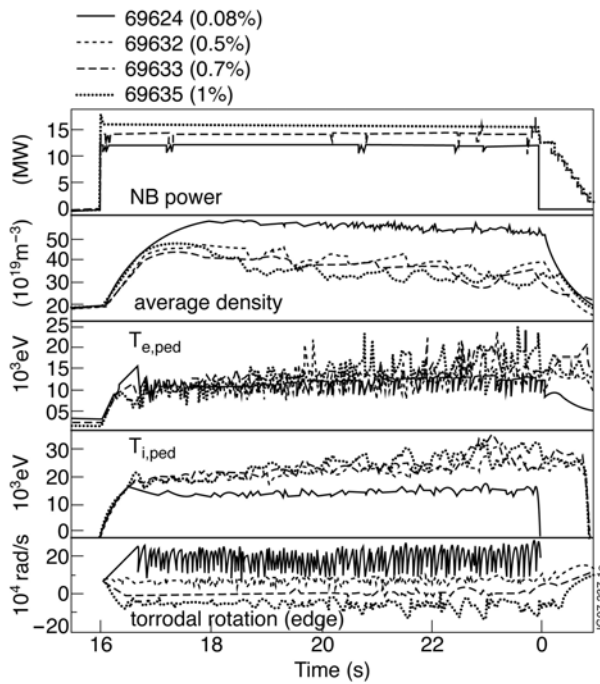


Figure 28: Experimental time traces for a 4-step ripple scan, with no gas fuelling in the H-mode phase (2.6MA/2.2T), at constant absorbed power ~ 12.5 -13MW (losses are up to 20% of input power). From top to bottom: NB input power, average density, pedestal electron, T_e , and ion, T_i , temperature and edge toroidal rotation .

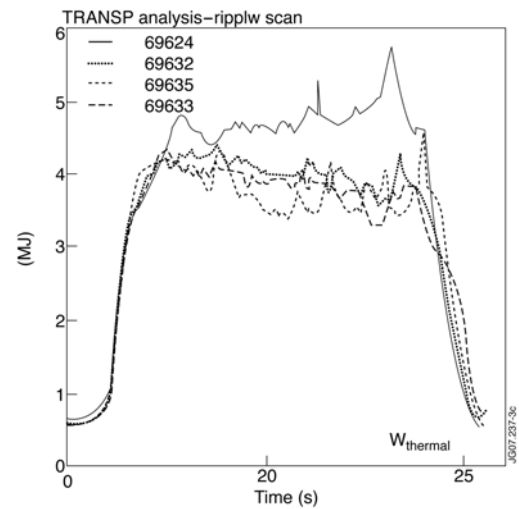


Figure 29: Plasma thermal stored energy, W_{th} , as calculated with TRANSP for the 4-step ripple scan in figure 28. Most of the W_{th} loss is already observed at $\delta_{BT}=0.5\%$.

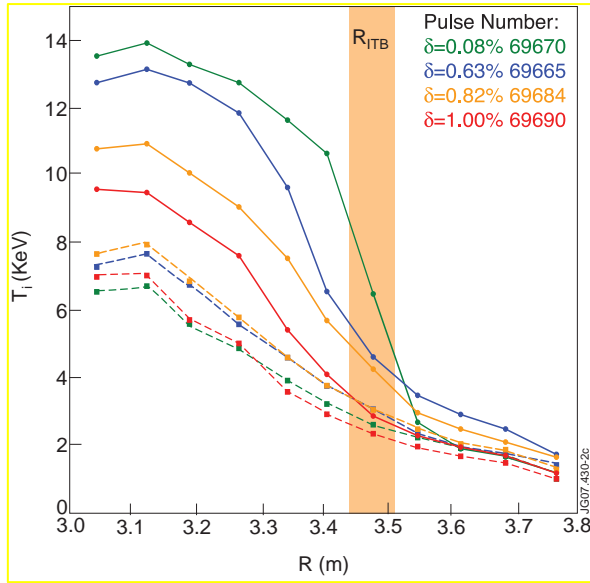


Figure 30: The ion temperature profiles as measured by the CXRS diagnostic for four discharges (reversed shear scenario) with equal absorbed power ($P_{\text{abs}} = 14.5 \pm 0.2 \text{ MW}$) taken at two times: at the time the ITB is triggered ($\sim t = 4.5 \text{ s}$) (dashed lines) and at the time of its maximum strength (solid lines). The centre of the plasma is at $R = 3.05 \text{ m}$ ($\rho = 0$) and the separatrix at $R = 3.85 \text{ m}$ ($\rho = 1$)

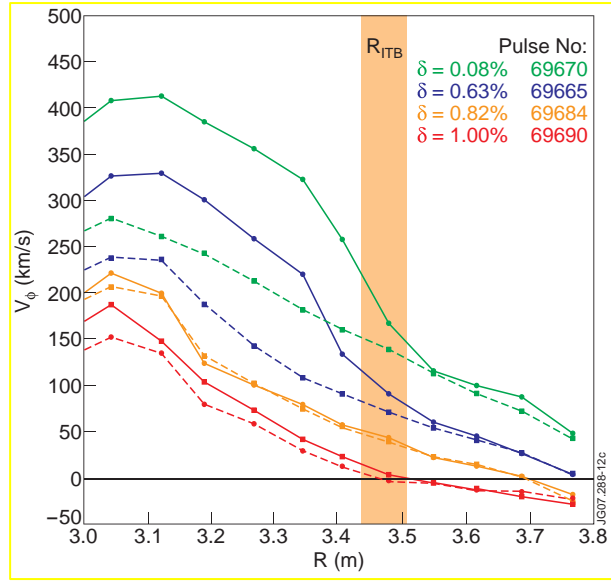


Figure 31: The toroidal rotation profiles (for carbon) as a function of the normalised poloidal flux, ρ , for the four discharges (reversed shear scenario) with equal absorbed power ($P_{\text{abs}} = 14.5 \pm 0.2 \text{ MW}$) taken at two times: at the time the ITB is triggered ($\sim t = 4.5 \text{ s}$) (dashed lines) and at the time of its maximum strength (solid lines). The centre of the plasma is at $R = 3.05 \text{ m}$ ($\rho = 0$) and the separatrix at $R = 3.85 \text{ m}$ ($\rho = 1$).

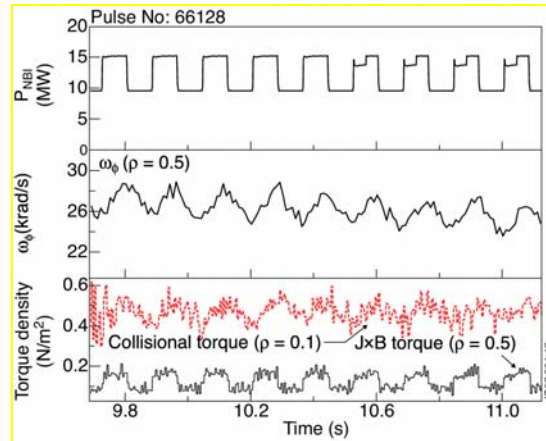


Figure 32: Time traces of modulated NB power (top), toroidal angular frequency ω_ϕ (middle) and two components of the torque density (bottom) for JET Pulse No. 66128.

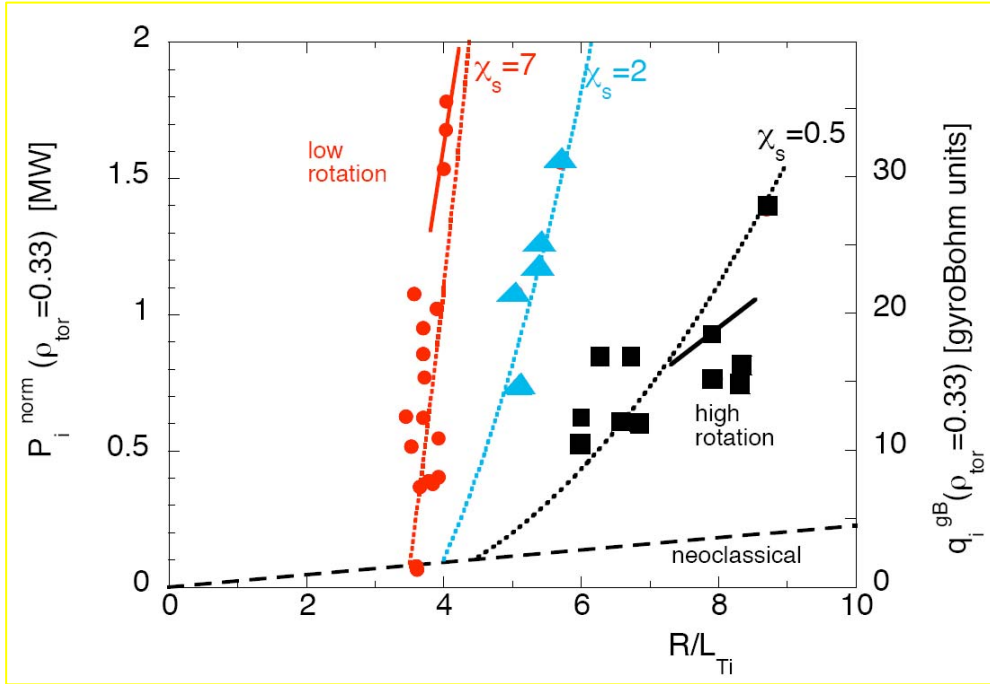


Figure 33: Normalised ion heat flux q_i at the square root of the normalised toroidal magnetic flux $\rho_{\text{tor}}=0.33$ vs the inverse ion temperature gradient length R/L_{Ti} for similar plasmas with different levels of rotation. Dots are experimental data and lines simulations.

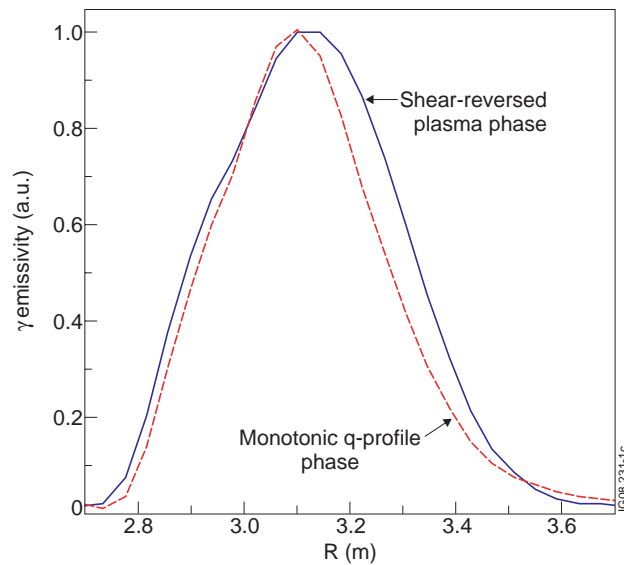


Figure 34: Mid-plane profiles of γ -ray emissivity obtained by tomographic reconstruction of the 2D γ -camera data for the ^3He -minority ICRH discharge #69436 ($I_p=2.3$ MA, $B_T=3.1$ T). solid line: shear-reversed plasma phase, $t=5.25$ s; dashed line: monotonic q-profile phase, $t=6.75$ s.

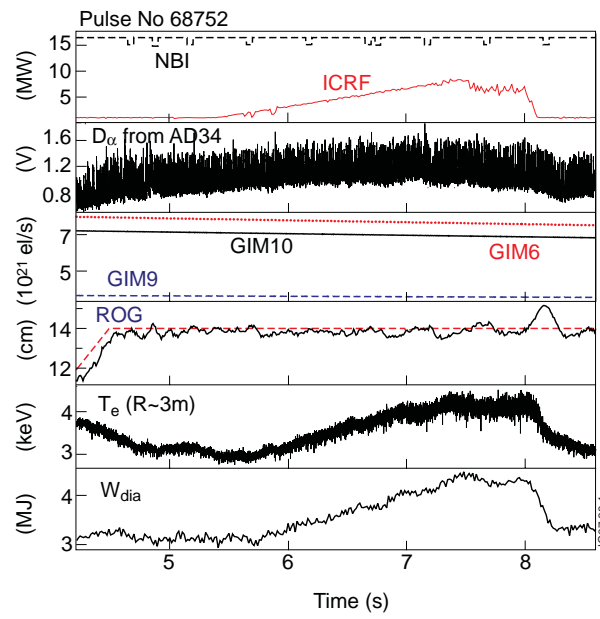


Figure 35: Illustration of high power ICRF coupling at large plasma-antenna distance in an ELMy H-Mode plasma. Shown are as a function of time: total ICRF power, D_α signal showing the ELM activity, gas puffing rate from the different gas inlets, position of the LCFS (ROG), central electron temperature and diamagnetic energy.

Appendix: List of JET-EFDA Contributors

G. Agarici³, M. Airila⁴⁶, R. Akers³⁷, Th. Alarcon³, R. Albanese²³, A. Alexeev⁶⁸, A. Alfier²², P. Allan³⁷, S. Almagia²⁶, A. Alonso⁵⁴, M. Alonso¹, B. Alper³⁷, H. Altmann³⁷, D. Alves¹, G. Ambrosino²³, V. Amosov⁶⁸, G. Anda⁵², F. Andersson¹⁹, E. Andersson-Sundén¹⁶, V. Andreev⁶¹, P. L. Andrew³⁷, Y. Andrew³⁷, M. Angelone²¹, A. Anghel⁶³, M. Anghel⁶², C. Angioni⁵⁶, G. Apruzzese²¹, N. Arcis³⁷, A. Argouach³, M. Ariola²³, A. Armitano³, R. Armstrong³⁴, G. Arnoux^{3, 37}, S. Arshad⁴⁴, G. Artaserse²³, J. F. Artaud³, A. Ash³⁷, E. Asp^{4, 35}, O. Asunta⁴⁶, C. V. Atanasiu⁶³, G. Atkins³⁷, M. D. Axton³⁷, A. Baciero⁵⁴, V. Bailescu⁶⁵, R. A. Baker³⁷, I. Balbao³⁷, N. Balshaw³⁷, J. W. Banks³⁷, Y. F. Baranov³⁷, D. Barbier^{3, 35}, I. L. Barlow³⁷, M. A. Barnard³⁷, R. Barnsley³³, L. Barrena⁵⁴, V. Basiuk³, G. Bateman⁵⁵, L. Baylor⁵⁹, P. S. Beaumont³⁷, K. Beausang³⁴, M. Bécoulet³, N. Bekris^{35, 43}, M. Beldishevski³⁷, A. C. Bell³⁷, F. Belli²¹, P. S. A. Belo¹, P. E. Bennett³⁷, N. A. Benterman³⁷, G. Berger-By³, T. Bergkvist²⁰, H. Berk⁶⁹, B. Bertrand³, M. N. A. Beurskens³⁷, B. Bieg⁷, T. M. Biewer⁵⁹, M. Bigi²², R. Bilato⁵⁶, J. Bizarro¹, T. R. Blackman³⁷, P. Blanchard⁵⁵, E. Blanco⁵⁴, J. Blum⁵³, V. Bobkov⁵⁶, A. Boboc³⁷, D. Boilson³⁴, T. Bolzonella²², G. Bonheure², X. Bonnin³, D. Borba^{1, 36}, A. Borthwick³⁷, C. Boulbe⁵³, C. Bourdelle³, K. v. Bovert⁴¹, M. Bowden³⁷, T. Boyce³⁷, H. J. Boyer³⁷, A. Bozhnikov⁴¹, R. J. Brade³⁷, J. M. A. Bradshaw³⁷, V. Braic⁶⁴, G. C. Braithwaite³⁷, B. Breizman⁶⁹, S. Bremond³, P. D. Brennan³⁷, J. Breue³⁹, S. Brezinsek⁴¹, M. D. J. Bright³⁷, F. Briscoe³⁷, M. Brix³⁷, M. Brombin²², B. C. Brown³⁷, D. P. D. Brown³⁷, J. Brzozowski²⁰, J. Bucalossi³, M. A. Buckley³⁷, T. Budd³⁷, R. V. Budny⁶⁰, P. Buratti²¹, G. Burcea⁶⁵, P. R. Butcher³⁷, R. J. Buttery³⁷, R. Cação¹, G. Calabrò²¹, C. P. Callaghan³⁷, P. G. Camp³⁷, D. C. Campling³⁷, J. Canik⁵⁹, A. J. Capel³⁷, P. J. Card³⁷, A. Cardinali²¹, P. Carman³⁷, D. Carralero⁵⁴, L. Carraro²², B. B. Carvalho¹, A. Casati³, C. Castaldo²¹, J. Caughman⁵⁹, R. Cavazzana²², M. Cavinato²², M. Cecconello^{15, 20}, F. E. Cecil³⁰, A. Cenedese²², C. Centioli²¹, R. Cesario²¹, C. D. Challis³⁷, M. Chandler³⁷, C. Chang⁵¹, A. Chankin⁵⁶, I. T. Chapman³⁷, D. J. Child³⁷, P. Chiru⁶³, G. Chitarin²², I. Chugonov⁵⁰, D. Ciric³⁷, R. H. Clarke³⁷, J. P. Coad³⁷, P. A. Coates³⁷, V. Coccoresse^{23, 35}, V. Cocilovo²¹, S. Coda⁴, R. Coelho¹, I. Coffey³³, L. Colas³, S. Collins³⁷, S. Combs⁵⁹, J. Compan⁴⁰, J. E. Conboy³⁷, S. Conroy¹⁵, N. Cook³⁷, S. P. Cook³⁷, D. Coombs³⁷, S. R. Cooper³⁷, Y. Corre³, G. Corrigan³⁷, S. Cortes¹, D. Coster⁵⁶, G. F. Counsell³⁷, X. Coutois³, M. Cox³⁷, T. Craciunescu⁶³, S. Cramp³⁷, F. Crisanti²¹, O. Croft³⁷, K. Crombe³¹, B. J. Crowley³⁷, N. Cruz¹, L. Cupido¹, M. Curuia⁶², R. A. Cusack³⁷, A. Czarnecka⁷, S. Dalley³⁷, E. T. Daly³⁷, A. Dalziel³⁷, D. Darrow⁶⁰, E. David⁶², O. David²⁸, N. Davies³⁷, J. J. Davis³⁷, C. Day⁴³, I. E. Day³⁷, M. R. de Baar³⁸, E. de La Luna⁵⁴, J. L. de Pablos⁵⁴, G. De Temmerman⁴, P. C. de Vries³⁷, R. De-Angelis²¹, F. Degli Agostini²², E. Delabie³⁸, D. del-Castillo-Negrete⁵⁹, L. Delpech³, A. J. Denyer³⁷, R. F. Denyer³⁷, G. De-Tommasi²³, S. Deveau⁵⁶, L. Di Matteo²¹, L. Di Pace²¹, P. J. Dirken³⁷, A. Dnestrovskiy⁶¹, K. Dominiczak³⁹, S. E. Dorling³⁷, D. Douai³, A. P. Down³⁷, P. T. Doyle³⁷, V. Drozdov³⁷, P. Dumortier², D. Dunai⁵², I. Duran⁶, F. Durodié², R. Eaton³⁷, T. Edlington³⁷, A. M. Edwards³⁷, D. T. Edwards³⁷, P. K. Edwards³⁷, Th. Eich⁵⁶, A. Ekedahl³, A. Elfimov¹, B. Ellingboe³⁴, C. G. Elsmore³⁷, B. Emmoth¹⁴, S. K. Erents³⁷, G. Ericsson¹⁵, A. Eriksson¹⁹, L. G. Eriksson³, B. Esposito²¹, H. G. Esser⁴¹, T. Estrada⁵⁴, E. A. Evangelidis⁵, G. E. Evans³⁷, G. D. Ewart³⁷, D. T. Ewers³⁷, G. Falchetto³, D. Falie⁶⁶, J. G. A. Fanthome³⁷, J. W. Farthing³⁷, A. Fasoli⁴, B. Faugeras⁵³, R. C. Felton³⁷, C. Fenzi³, H. Fernandes¹, J. A. Ferreira⁵⁴, J. Ferreira¹, J. Ferron⁴⁵, J. A. Fessey³⁷, L. Figini²⁴, A. Figueiredo¹, J. Figueiredo¹, P. Finburg³⁷, K. H. Finken⁴¹, U. Fischer⁴³, N. Fitzgerald³⁴, J. Flanagan³⁷, C. Fleming³⁷, A. Fonseca¹, A. D. Forbes³⁷, O. Ford⁴⁷, D. Fraboulet^{3, 35}, R. J. Francis³⁷, J. P. Friconeau²⁸, D. Frigione^{21, 35}, J. C. Fuchs⁵⁶, K. Fullard³⁷, W. Fundamenski³⁷, J. Gafert⁵⁶, K. Gál⁵², R. Galvão¹, S. Garavaglia²⁴, X. Garbet³, J. Garcia³, M. Garcia

Munoz⁵⁶, W. Gardner⁵⁹, D. Garnier³, L. Garzotti³⁷, M. Gatu-Johnson¹⁵, E. Gauthier³, J. W. Gaze³⁷, D. F. Gear³⁷, J. Gedney³⁷, S. J. Gee³⁷, E. Genangeli^{21, 35}, S. Gerasimov³⁷, A. Geraud³, M. Gherendi⁶³, C. S. Gibson³⁷, S. J. Gilligan³⁷, C. G. Gimblett³⁷, D. Gin⁵⁰, E. Giovannozzi²¹, C. Giroud³⁷, G. Giruzzi³, S. Glowacz⁷, J. Godwin³⁷, J. K. Goff³⁷, P. Gohil⁴⁵, V. Goloborod'ko¹⁰, B. Gonçalves¹, M. Goniche³, A. Goodyear³⁷, N. Gorelenkov⁶⁰, G. Gorini²⁴, R. Goulding⁵⁹, B. Graham³⁷, D. Graham³⁷, M. E. Graham³⁷, G. Granucci²⁴, J. Graves⁴, N. R. Green³⁷, H. Greuner⁵⁶, E. Grigore⁶³, F. S. Griph³⁷, C. Grisolia³, G. Gros³, G. Grossetti²⁴, S. Grünhagen⁴³, M. P. Gryaznevich³⁷, R. Guirlet³, B. Gulejova⁴, J. Gunn³, P. Guzdar⁴⁸, P. Hacek⁶, L. J. Hackett³⁷, S. Hacquin³, B. Haist³⁷, A. Hakola⁴⁶, S. J. Hall³⁷, S. P. Hallworth Cook³⁷, D. T. Hamilton³⁷, R. C. Handley³⁷, S. Harding³⁷, J. D. W. Harling³⁷, M. J. Harvey³⁷, T. D. V. Haupt³⁷, N. C. Hawkes³⁷, J. H. Hay³⁷, N. Hayashi⁵¹, P. W. Haydon³⁷, I. R. Hayward³⁷, P. J. L. Heesterman³⁷, W. Heidbrink⁶⁰, J. Heikkinen⁷¹, C. Hellesen¹⁵, T. Hellsten²⁰, O. N. Hemming³⁷, T. C. Hender³⁷, V. Hennion^{3, 35}, C. Hidalgo⁵⁴, S. Higashijima⁵¹, J. W. Hill³⁷, K. Hill⁶⁰, M. Hill³⁷, J. Hillairet³, D. Hillis⁵⁹, T. Hirai⁴⁰, M. Hitchin³⁷, J. Hobirk⁵⁶, C. Hogan⁵⁹, C. H. A. Hogben³⁷, G. M. D. Hogeweyj³⁸, I. C. Hollingham³⁷, K. Holmström²⁰, D. A. Homfray³⁷, G. Honeyands³⁷, S. H. Hong³, C. Hopf⁵⁶, B. A. Horn³⁷, A. R. Horton³⁷, L. D. Horton⁵⁶, S. P. Hotchin³⁷, M. R. Hough P³⁷, W. Houlberg⁵⁹, D. F. Howell³⁷, M. Hron⁶, A. Huber⁴¹, T. M. Huddleston³⁷, Z. Hudson³⁷, M. Hughes³⁷, M. Hühnerbein³⁹, C. C. Hume³⁷, A. J. Hunt³⁷, C. L. Hunter³⁷, T. S. Hutchinson³⁷, S. Huygen², G. Huysmans³, V. Hynönen⁴⁶, S. Ide⁵¹, R. Igreja¹, F. Imbeaux³, E. Iivings³⁷, S. Jachmich², G. Jackson⁴⁵, P. Jacquet³⁷, K. Jakubowska¹⁸, M. Jakubowski^{41, 57}, P. V. James³⁷, R. J. E. Jaspers³⁸, S. Jednorog⁷, I. Jenkins³⁷, M. A. C. Jennison³⁷, C. Jeskins³⁷, E. Joffrin^{3, 35}, M. F. Johnson³⁷, R. Johnson³⁷, T. Johnson²⁰, D. Jolovic⁴¹, E. M. Jones³⁷, G. Jones³⁷, H. D. Jones³⁷, T. T. C. Jones³⁷, C. Jupén¹⁷, I. Kachtchouk⁶⁸, J. Kaczmarczyk⁷, J. Källne¹³, D. Kalupin⁴¹, S. Kálvin⁵², G. Kamelander¹⁰, R. Kamendje^{9, 35}, S. Karttunen⁷¹, I. Katramados³⁷, M. Kaufmann⁵⁶, G. Kaveney³⁷, A. S. Kaye³⁷, M. J. Kear³⁷, D. L. Keeling³⁷, D. Kelliher³⁴, N. G. Kidd³⁷, R. F. King³⁷, D. J. Kinna³⁷, V. Kiptily³⁷, G. Kirnev⁶¹, N. Kirneva⁶¹, A. Kirschner⁴¹, G. Kiss⁴¹, T. Kiviniemi⁴⁶, A. Klein⁵⁸, M. Knaup⁴¹, K. kneuper³⁷, H. Kneupner⁴¹, P. J. Knight³⁷, S. J. Knipe³⁷, M. Kocan³, F. Köchl¹⁰, G. Kocsis⁵², C. Konz⁵⁶, T. Koppitz⁴², A. Korotkov³⁷, H. R. Koslowski⁴¹, V. Kotov⁴¹, M. D. Kovari³⁷, K. Kovarik⁶, G. Kramer⁶⁰, A. Krasilnikov⁶⁸, V. Krasilnikov⁶⁸, A. Kreter⁴¹, K. Krieger⁵⁶, A. Kritz⁵⁵, Y. Krivchenkov³⁷, M. Krychowiak⁵⁷, S. Krylov⁶¹, I. Ksiazek⁷, M. Kubic⁶, S. Kuhn¹⁰, W. Kühnlein³⁹, T. Kurki-Suonio⁴⁶, A. Kurowski⁷, B. Kuteev⁶¹, R. La Haye⁴⁵, A. Lachichi³⁷, N. Lam³⁷, P. Lang⁵⁶, M. T. Large³⁷, I. Lassiwe⁴¹, J. R. Last³⁷, L. Lauro Taroni²², K. D. Lawson³⁷, M. Laxåback^{20, 35}, R. A. Layne³⁷, E. Lazzaro²⁴, F. Le Guern³, B. LeBlanc⁶⁰, H. J. Leggate³⁷, M. Lehnen⁴¹, I. Lengar⁸, M. Lennholm³, E. Lerche², C. N. Lescure³⁷, A. Li Puma³, Y. Liang⁴¹, J. Likonen⁷¹, J. Linke⁴⁰, S. A. Linstead³⁷, X. Litaudon³, Y. Liu³⁷, Y. Q. Liu¹², C. Llewellyn Smith³⁷, T. Loarer³, R. C. Lobel³⁷, P. J. Lomas³⁷, F. D. Long³⁷, J. Lönnroth⁴⁶, D. J. Looker³⁷, M. J. Loughlin³⁷, A. B. Loving³⁷, T. Luce⁴⁵, R. M. A. Lucock³⁷, A. M. Lungu⁶³, C. P. Lungu⁶³, P. Macheta³⁷, A. S. Mackenzie³⁷, M. Macrae³⁷, G. Maddaluno²¹, G. P. Maddison³⁷, J. Madsen¹¹, P. Maget³, C. Maggi⁵⁶, H. Maier⁵⁶, J. Mailloux³⁷, M. Makowski⁴⁵, C. J. Manning³⁷, M. Mansfield³⁴, M. E. Manso¹, P. Mantica²⁴, M. Mantsinen⁴⁶, M. Maraschek⁵⁶, C. Marchetto²⁴, M. A. Marchitti²³, J. L. Marechal³, M. Marinelli²⁶, A. Marinoni⁴, M. Marinucci²¹, J. Märki⁴, D. Marocco²¹, C. A. Marren³⁷, D. L. Martin³⁷, D. Martin³⁷, G. Martin^{3, 35}, Y. Martin⁴, K. Masaki⁵¹, M. Maslov⁴, A. Matilal³⁷, M. Mattei²³, G. F. Matthews³⁷, A. Maviglia²³, C. R. May³⁷, M. Mayer⁵⁶, M. L. Mayoral³⁷, D. Mazon³, C. Mazzotta²¹, E. Mazzucato⁶⁰, P. McCarthy³⁴, K. G. McClements³⁷, K. McCormick⁵⁶, P. A. McCullen³⁷, D. McCune⁶⁰, D. C. McDonald³⁷, R. McGregor³⁷, J. P. Mckivitt³⁷, A.

Meakins³⁷, F. Medina⁵⁴, A. G. Meigs³⁷, M. Menard⁴⁵, L. Meneses¹, S. Menmuir¹⁸, I. R. Merrigan³⁷, Ph. Mertens⁴¹, A. Messiaen², H. Meyer³⁷, A. G. Miller³⁷, S. F. Mills³⁷, J. J. Milnes³⁷, T. Mindham³⁷, F. Mirizzi²¹, R. Mitteau³, J. Mlynar⁶, P. Mollard³, I. Monakhov³⁷, P. Monier-Garbet³, R. Mooney³⁷, S. Moradi⁶⁷, D. Moreau³, Ph. Moreau³, L. Moreira³⁷, A. Morgan³⁷, P. D. Morgan³⁷, C. Morlock^{35, 41}, A. W. Morris³⁷, G. L. Mort³⁷, C. Mrozek^{35, 56}, A. Mueck⁴, H. W. Müller⁵⁶, M. Murakami⁵⁹, A. Murari²², I. Mustata⁶³, F. Nabais¹, E. Nardon³⁷, E. Nardon³, G. Nash³⁷, V. Naulin¹¹, M. F. F. Nave¹, R. Nazikian⁶⁰, I. Nedzelski¹, C. R. Negus³⁷, J. D. Neilson³⁷, A. Neto¹, R. Neu⁵⁶, O. Neubauer⁴¹, G. J. Newbert³⁷, M. Newman³⁷, K. J. Nicholls³⁷, A. Nicolai⁴¹, L. Nicolas³, P. Nieckchen^{35, 56}, A. H. Nielsen¹¹, S. K. Nielsen¹¹, M. P. S. Nightingale³⁷, C. Noble³⁷, M. Nora⁴⁶, H. Nordman¹⁹, M. Norman³⁷, C. Norris^{35, 37}, J-M. Noterdaeme⁵⁶, S. Nowak²⁴, I. Nunes^{1, 35}, F. Ognissanto²⁴, T. O'Gorman³⁴, A. Oleynikov⁶⁸, M. O'Mullane³², J. Ongena², F. Orsitto²¹, O. I. Oswuigwe³⁷, M. Ottaviani³, N. Oyama⁵¹, D. Pacella²¹, K. Paget³⁷, J. Pamela³, J. Paméla³⁶, R. Panek⁶, L. Pangione³⁷, A. Panin⁴¹, Th. Panis⁴, A. Pankin⁶⁰, A. Pantea⁶³, V. Parail³⁷, Th. Parisot³, A. Parkin³⁷, A. Parsloe³⁷, B. T. Parsons³⁷, R. Pasqualotto²², P. Pastor³, R. Paterson³⁷, D. Peach³⁷, R. J. H. Pearce³⁷, B. J. Pearson³⁷, I. J. Pearson³⁷, L. C. Pedrick³⁷, M. A. Pedrosa⁵⁴, B. Pegourie³, R. Pereira¹, E. Perelli Cippo²⁴, G. Pereverzev⁵⁶, A. Perevezentsev³⁷, C. Perez von Thun³⁷, Ch. Perez von Thun⁵⁶, V. Pericoli-Ridolfini²¹, A. Perona²⁵, Y. Perrot²⁸, S. Peruzzo²², G. Petravich⁵², L. Petrizzi²¹, V. Petrov⁶⁸, V. Petrzilka⁶, V. Phillips⁴¹, G. Piazza⁴³, F. Piccolo³⁷, A. Pietropaolo²⁴, M. Pillon²¹, S. D. Pinches³⁷, T. Pinna²¹, G. Pintsuk⁴⁰, A. Pironti²³, R. Pitts⁴, V. Plyusnin¹, N. Pomaro²², O. Pompilian⁶³, L. Poncet³, P. J. Pool³⁷, S. Popovichev³⁷, F. Porcelli²⁵, M. T. Porfiri²¹, C. Portafaix³, A. Pospieszczyk⁴¹, G. Prestopino²⁶, P. Prior³⁷, R. Prokopowicz⁷, I. Proverbio²⁴, R. Pugno⁵⁶, M. E. Puiatti²², K. Purahoo³⁷, V. Pustovitov⁶⁸, Th. Pütterich⁵⁶, D. Püttmann-Kneupner⁴¹, A. Quercia²³, E. Rachlew¹⁸, M. S. J. Rainford³⁷, G. Ramogida²¹, K. Rantamäki⁷¹, J. Rapp⁴¹, J. J. Rasmussen¹¹, G. Rattá⁵⁴, G. Ravera²¹, M. Reich⁵⁶, R. Reichle³, R. Reiss³, D. Reiter⁴¹, D. Rendell³⁷, C. Reux³, T. T. Ribeiro¹, V. Riccardo³⁷, F. G. Rimini³, M. Riva²¹, J. E. C. Roberts³⁷, R. J. Robins³⁷, D. S. Robinson³⁷, S. A. Robinson³⁷, D. W. Robson³⁷, H. Roche³, M. Rödig³⁹, V. Rohde⁵⁶, A. Rolfe³⁷, F. Romanelli^{21, 35}, M. Romanelli³⁷, A. Romano²¹, J. Romero⁵⁴, E. Ronchi¹⁵, S. Rosanvallon³, Ch. Roux³, S. Rowe³⁷, M. Rubel²⁰, L. Ruchko¹, C. Ruset⁶³, M. Russell³⁷, A. Ruth³⁴, L. Ryc⁷, A. Rydzy²¹, F. Ryter⁵⁶, J. Rzadkiewicz⁷, S. Saarelma³⁷, F. Sabathier³, R. Sabot³, S. Sadakov⁴¹, P. Sagar³⁷, G. Saibene⁴⁴, A. Saille³, F. Saint-Laurent³, M. Tsalas³⁵, A. Salmi⁴⁶, R. Salomaa⁴⁶, F. Salzedas¹, U. Samm⁴¹, S. G. Sanders³⁷, S. Sanders³⁷, G. Sandford³⁷, K. Sandland³⁷, P. Sandquist¹⁹, D. E. G. Sands³⁷, M. I. K. Santala⁴⁶, F. Sartori³⁷, R. Sartori⁴⁴, O. Sauter⁴, A. Savelyev²³, A. Savtchikov⁴¹, S. C. Scales³⁷, A. Scarabosio^{4, 56}, N. Schaefer³, Ch. Schlatter⁴, V. Schmidt²², M. Schneider³, M. Scholz⁷, K. Schöpf¹⁰, B. Schweer⁴¹, J. Schweinzer⁵⁶, M. Seki⁵¹, L. Semeraro²¹, A. Semerok²⁹, G. Sergienko⁴¹, F. Serra¹, M. Sertoli⁵⁶, M. M. J. Shannon³⁷, S. E. Sharapov³⁷, S. R. Shaw³⁷, A. Shevelev⁵⁰, R. Sievering⁴², C. A. Silva¹, P. A. Simmons³⁷, A. Simonetto²⁴, D. Simpson³⁷, S. Sipila⁴⁶, A. C. C. Sips⁵⁶, A. Sirinelli³, H. Sjöstrand¹⁵, D. Skopintsev⁶⁸, P. G. Smith³⁷, J. Snipes⁵⁸, L. Snoj⁸, S. Snyder⁵⁵, S. Soare⁶², E. R. Solano⁵⁴, P. Sonato²², A. Sopplesa²², J. Sousa¹, C. B. C. Sowden³⁷, C. Sozzi²⁴, T. Spelzini³⁷, J. Spence³⁷, F. Spineanu⁶³, P. Spuig³, A. Stäbler⁵⁶, R. D. Stagg³⁷, M. F. Stamp³⁷, V. Stancalie⁶³, P. Stangeby⁴⁵, D. E. Starkey³⁷, M. J. Stead³⁷, A. V. Stephen³⁷, A. L. Stevens³⁷, J. Stober⁵⁶, R. B. Stokes³⁷, D. Stork³⁷, D. Stoyanov²⁷, J. Strachan⁶⁰, P. Strand¹⁹, D. Strintzi⁵, W. Studholme³⁷, F. Subba²⁵, H. P. Summers³², P. Sundelin²⁰, C. Surdu-Bob⁶³, E. Surrey³⁷, D. J. Sutton³⁷, J. Svensson⁵⁶, D. Swain⁵⁹, B. D. Syme³⁷, I. D. Symonds³⁷, T. Szepesi⁵², A. Szydlowski⁷, F. Tabares⁵⁴, H. Takenaga⁵¹, T. Tala⁷¹, A. R. Talbot³⁷, C. Taliercio²², C. Tame³⁷, G.

Tardini ⁵⁶, M. Tardocchi ²⁴, G. Telesca ², A. O. Terrington ³⁷, D. Testa ⁴, J. M. Theis ³, J. D. Thomas ³⁷, P. D. Thomas ³⁷, P. R. Thomas ⁴⁴, V. K. Thompson ³⁷, A. Thyagaraja ³⁷, P. A. Tigwell ³⁷, I. Tiseanu ⁶³, J. M. Todd ³⁷, T. N. Todd ³⁷, M. Z. Tokar ⁴¹, P. Trabuc ³, J. M. Traver ³, W. Treutterer ⁵⁶, A. Trkov ⁸, M. Tsalas ⁵, H. Tsige-Tamirat ⁴³, E. Tsitrone ³, D. Tskhakaya ^{jun} ¹⁰, O. Tudisco ²¹, S. Tugarinov ⁶⁸, M. M. Turner ³⁴, G. Turri ⁴, S. G. J. Tyrrell ³⁷, N. Umeda ⁵¹, B. Unterberg ⁴¹, H. Urano ⁵¹, A. J. Urquhart ³⁷, I. Uytendhoven ⁴⁰, A. P. Vadgama ³⁷, G. Vagliasindi ²¹, M. Valisa ²², M. Valovic ³⁷, D. Van Eester ², B. van Milligen ⁵⁴, G. J. van Rooij ³⁸, C. A. F. Varandas ¹, S. Vartanian ³, J. Vega ⁵⁴, J. M. Verger ³, C. Verona ²⁶, Th. Versloot ³⁸, M. Vervier ², S. Villari ²¹, E. Villedieu ³, F. Villone ²³, J. E. Vince ³⁷, G. J. Vine ³⁷, E. Vitale ²¹, M. Vlad ⁶³, I. Voitsekhovitch ³⁷, M. Vrancken ², K. Vulliez ³, A. D. Walden ³⁷, C. W. F. Waldon ³⁷, M. Walker ³⁷, M. J. Walsh ³⁷, J. Waterhouse ³⁷, M. L. Watkins ^{35, 37}, M. J. Watson ³⁷, M. W. Way ³⁷, C. R. Webb ³⁷, J. Weiland ¹⁹, H. Weisen ⁴, M. Weiszflog ¹⁵, R. Wenninger ^{35, 56}, A. T. West ³⁷, J. M. Weulersse ²⁹, B. Weyssow ³⁶, M. R. Wheatley ³⁷, A. D. Whiteford ³², A. M. Whitehead ³⁷, A. G. Whitehurst ³⁷, A. M. Widdowson ³⁷, R. C. Wieggers ³⁸, S. Wiesen ⁴¹, A. Wilson ³⁷, D. J. Wilson ³⁷, D. Wilson ³⁷, H. R. Wilson ^{37, 70}, M. Wischmeier ⁵⁶, D. M. Witts ³⁷, R. C. Wolf ⁴¹, G. M. Wright ³⁸, V. Yavorskij ¹⁰, J. Yorkshades ³⁷, C. Young ³⁷, D. Young ³⁷, I. D. Young ³⁷, X. Yuhong ², L. Zabeo ³⁷, A. Zabolotsky ⁴, R. Zagorski ^{7, 36}, L. Zakharov ⁶⁰, R. Zanino ²⁵, V. Zaroschi ⁶³, K. D. Zastrow ³⁷, B. Zefran ⁸, W. Zeidner ⁵⁶, M. Zerbini ²¹, Y. Zhu ⁴⁹, O. Zimmermann ⁴¹, V. Zoita ⁶³, S. Zoletnik ⁵², W. Zwingman ³

¹ Associação EURATOM/IST, Instituto de Plasmas e Fusão Nuclear, Instituto Superior Técnico, Av Rovisco Pais, 1049-001 Lisbon, Portugal,

² Association "EURATOM - Belgian State" Laboratory for Plasma Physics Koninklijke Militaire School - Ecole Royale Militaire Renaissancelaan 30 Avenue de la Renaissance B-1000 Brussels Belgium,

³ Association EURATOM-CEA, CEA/DSM/IRFM, Cadarache 13108 Saint Paul Lez Durance, France,

⁴ Association EURATOM-Confédération Suisse, Ecole Polytechnique Fédérale de Lausanne (EPFL), CRPP, CH-1015 Lausanne, Switzerland,

⁵ Association EURATOM-Hellenic Republic, NCSR "Demokritos"153 10, Agia Paraskevi Attica, Greece,

⁶ Association EURATOM-IPP.CR, Institute of Plasma Physics AS CR, Za Slovankou 3, 182 21 Praha 8, Czech Republic,

⁷ Association Euratom-IPPLM, Hery 23, 01-497 Warsaw, Poland,

⁸ Association EURATOM-MHST, Jozef Stefan Institute, Reactor Physics Department, Jamova 39, SI-1000 Ljubljana,

⁹ Association EURATOM-ÖAW, Institut für Theoretische Physik-Computational Physics, Technische Universität Graz, Petersgasse 16, A- 8010 Graz, Austria,

¹⁰ Association EURATOM-Österreichische Akademie der Wissenschaften (ÖAW), Austria,

¹¹ Association EURATOM-Risø National Laboratory, Technical University of Denmark, P.O.Box 49, DK-4000 Roskilde, Denmark,

¹² Association EURATOM-VR, Department of Applied Mechanics, Chalmers University of Technology, SE-41296 Gothenburg, Sweden,

¹³ Association EURATOM-VR, Department of Engineering Sciences, Uppsala University, SE-75120 Uppsala, Sweden ,

¹⁴ Association EURATOM-VR, Department of Material Physics, ICT, KTH, SE-16440 Kista, Sweden,

¹⁵ Association EURATOM-VR, Department of Physics and Astronomy, Uppsala University, SE-75120 Uppsala, Sweden,

- ¹⁶ Association EURATOM-VR, Department of Physics and Astronomy, Uppsala University, SE-75120 Uppsala, Sweden ,
- ¹⁷ Association EURATOM-VR, Department of Physics, Lund University, SE-22100 Lund, Sweden,
- ¹⁸ Association EURATOM-VR, Department of Physics, SCI, KTH, SE-10691 Stockholm, Sweden,
- ¹⁹ Association EURATOM-VR, Department of Radio and Space Science, Chalmers University of Technology, SE-41296 Gothenburg, Sweden,
- ²⁰ Association EURATOM-VR, Fusion Plasma Physics, EES, KTH, SE-10044 Stockholm, Sweden,
- ²¹ Associazione EURATOM-ENEA sulla Fusione, C.R. Frascati, Roma, Italy,
- ²² Associazione EURATOM-ENEA sulla Fusione, Consorzio RFX Padova, Italy,
- ²³ Associazione EURATOM-ENEA sulla Fusione, CREATE, Italy.,
- ²⁴ Associazione EURATOM-ENEA sulla Fusione, IFP Milano, Italy,
- ²⁵ Associazione EURATOM-ENEA sulla Fusione, Politecnico di Torino, Italy,
- ²⁶ Associazione EURATOM-ENEA sulla Fusione, Università di Roma, Italy,
- ²⁷ Bulgarian Academy of Sciences, 6 Moskovsak Str., Sofia 1000, Bulgaria,
- ²⁸ CEA/Fontenay aux Roses, B.P.6 F-92265 Fontenay-aux-roses CEDEX, France,
- ²⁹ CEA/Saclay, F-91191 Gif-sur-Yvette CEDEX, France,
- ³⁰ Colorado School of Mines, 1500 Illinois Street, Golden, CO 80401, Colorado, USA,
- ³¹ Department of Applied Physics UG (Ghent University) Rozier 44 B-9000 Ghent Belgium,
- ³² Department of Physics and Applied Physics, University of Strathclyde, Glasgow, G4 ONG, UK,
- ³³ Department of Pure and Applied Physics, Queens University, Belfast, BT7 1NN, UK,
- ³⁴ Dublin City University (DCU), Ireland,
- ³⁵ EFDA Close Support Unit, Culham Science Centre, Culham, OX14 3DB, UK,
- ³⁶ EFDA Close Support Unit, D-85748 Garching, Germany,
- ³⁷ Euratom/UKAEA Fusion Association, Culham Science Centre, Abingdon, Oxon, OX14 3DB, UK.,
- ³⁸ FOM Institute for Plasma Physics Rijnhuizen, Association EURATOM-FOM, Trilateral Euregio Cluster, The Netherlands, (www.rijnh.nl),
- ³⁹ Forschungszentrum Jülich GmbH, Fachbereich Betriebsdirektion, D-52425 Jülich, Germany ,
- ⁴⁰ Forschungszentrum Jülich GmbH, Institut für Energieforschung - Werkstoffstruktur und Eigenschaften, EURATOM-Assoziation, D-52425 Jülich, Germany,
- ⁴¹ Forschungszentrum Jülich GmbH, Institut für Plasmaphysik, EURATOM-Assoziation, Trilateral Euregio Cluster, D-52425 Jülich, Germany,
- ⁴² Forschungszentrum Jülich GmbH, Zentralabteilung Technologie, D-52425 Jülich, Germany,
- ⁴³ Forschungszentrum Karlsruhe GmbH, P.O.Box 3640, D-76021 Karlsruhe, Germany,
- ⁴⁴ Fusion for Energy Joint Undertaking, Josep Pl. 2, Torres Diagonal Litoral B3, 08019, Barcelona, Spain,
- ⁴⁵ General Atomics, P.O.Box 85608, San Diego, CA 92186-5608, California, USA,
- ⁴⁶ Helsinki University of Technology, Association EURATOM-Tekes, P.O.Box 4100, FIN-02015 TKK, Finland,
- ⁴⁷ Imperial College, University of London, London, SW7 2AZ, UK,
- ⁴⁸ Institute for Plasma Research, University of Maryland, College Park, MD 20742-3511, Maryland, USA,
- ⁴⁹ Institute of Plasma Physics, Chinese Academy of Sciences Hefei 230031 China,
- ⁵⁰ Ioffe Physico-Technical Institute, 26 Politekhnikeskaya, St Petersburg 194021, Russian Federation,

- ⁵¹ Japan Atomic Energy Agency, Naka Fusion Research Establishment, Nakamachi, Nakagun, Ibaraki-ken 311-0913, Japan,
- ⁵² KFKI-Research Institute for Particle and Nuclear Physics, Association EURATOM, P.O.Box 49, H-1525, Budapest, Hungary,
- ⁵³ Laboratoire J.A.Dieudonné, Université de Nice-Sophia-Antipolis, Parc Valrose, F-06108 Nice CEDEX 02, France,
- ⁵⁴ Laboratorio Nacional de Fusion, Asociacion EURATOM-CIEMAT, Madrid, Spain,
- ⁵⁵ Lehigh University, Bethlehem, PA 18015, Pennsylvania, USA,
- ⁵⁶ Max-Planck-Institut für Plasmaphysik, EURATOM-Assoziation, D-85748 Garching, Germany,
- ⁵⁷ Max-Planck-Institut für Plasmaphysik, Teilinstitut Greifswald, EURATOM-Assoziation, D-17491 Greifswald, Germany,
- ⁵⁸ MIT Plasma Science and Fusion Centre, Cambridge, MA 02139, Massachusetts, USA,
- ⁵⁹ Oak Ridge National Laboratory, Oak Ridge, TN 37831-6169, Tennessee, USA,
- ⁶⁰ Princeton Plasma Physics Laboratory, James Forrestal Campus, Princeton, NJ 08543, New Jersey, USA,
- ⁶¹ RRC Kurchatov Institute, 1 Kurchatov Square, Moscow 123182, Russian Federation,
- ⁶² The National Institute for Cryogenics and Isotopic Technology, Association EURATOM-MEdC, Ramnicu Valcea, Romania,
- ⁶³ The National Institute for Laser, Plasma and Radiation Physics, Association EURATOM-MEdC, Magurele-Bucharest, Romania,
- ⁶⁴ The National Institute for Optoelectronics, Magurele-Bucharest, Romania, Association EURATOM-MEdC,
- ⁶⁵ The Nuclear Fuel Plant, Pitesti, Romania,
- ⁶⁶ The Politehnica University, Bucharest, Romania,
- ⁶⁷ Theoretical and Mathematical Physics, Statistical and Plasma Physics Unit, Association EURATOM-Belgian State, Université Libre de Bruxelles, Campus Plaine, CP 231, Boulevard du Triomphe, B-1050 ,
- ⁶⁸ Troitsk Institute of Innovating and Thermonuclear Research (TRINITI), Troitsk 142190, Moscow Region, Russian Federation,
- ⁶⁹ University of Texas at Austin, Institute for Fusion Studies, Austin, TX 78712, Texas, USA,
- ⁷⁰ University of York, Heslington, York YO10 5DD UK.,
- ⁷¹ VTT Technical Research Centre of Finland, Association EURATOM-Tekes, P.O.Box 1000, FIN-02044 VTT, Finland